Volume 41
DOE/DP40200-112

LLE Review

Quarterly Report

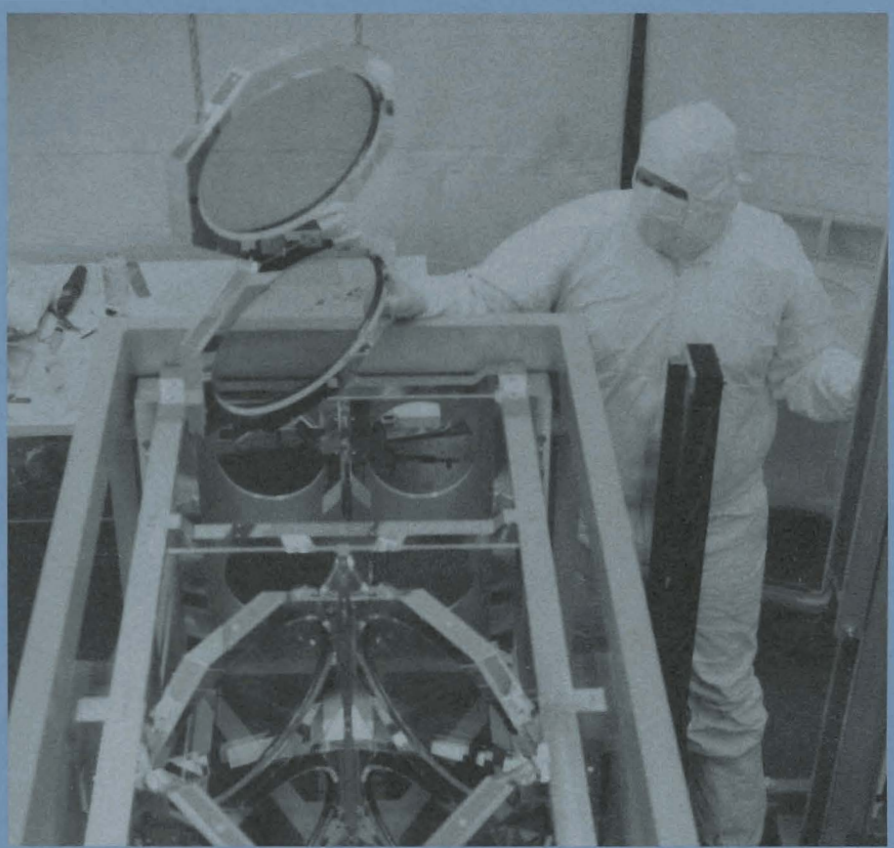

October–December 1989

Laboratory for Laser Energetics
College of Engineering and Applied Science
University of Rochester
250 East River Road
Rochester, New York 14623-1299

UR
LLE

Volume 41
DOE/DP40200-112

LLE Review

Quarterly Report

Editor: D.K. Bradley
(716) 275-5769

October–December 1989

Laboratory for Laser Energetics
College of Engineering and Applied Science
University of Rochester
250 East River Road
Rochester, New York 14623-1299

IN BRIEF

This volume of the LLE Review, covering the period October–December 1989, contains an article discussing saturation effects and power-balance considerations in the design of high-power lasers and an article describing numerical modeling of the effects of power imbalances on target behavior. The advanced technology section reports on (1) the development of a liquid crystal laser-beam apodizer and (2) an experiment to study the high-intensity ionization of noble gases. Finally, the activities of the National Laser Users Facility and the GDL and OMEGA laser facilities are summarized.

The highlights of this issue are

- The problem of achieving power balance in high-efficiency, multibeam lasers has been studied in terms of gain-saturation effects and the nonlinear nature of harmonic frequency conversion. It is shown that power imbalance can be minimized by balancing the gains and losses in equivalent amplification stages in each beamline.

- The effects of target implosion behavior of various power-imbalance sources in the OMEGA laser system have been studied using the two-dimensional hydrodynamics code *ORCHID*. The simulations show good agreement with an experiment in which a deliberate power imbalance was applied to the target drive.

- Laser-beam apodizers with large clear apertures have been fabricated using cholesteric liquid crystals. A soft-edge profile has been achieved by filling a cell with two separate liquid crystals with different selective-reflection bands, and allowing them to partially mix at the interface.

- A study of the ionization of noble gases in the tunneling regime using high-intensity, 1-ps pulses from the tabletop terawatt laser (T^3) has been carried out. The measured ion production is well predicted by a Coulomb barrier suppression ionization theory.

CONTENTS

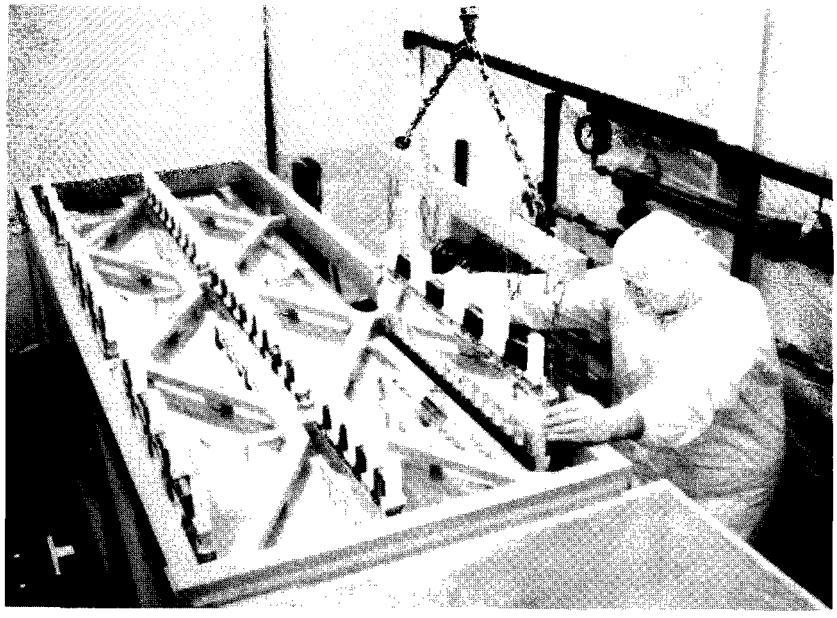

Milton Shoup III, a Technical Associate in the Engineering Division, shown assembling the Multisegmented Amplifier (MSA) prototype. This amplifier consists of a 2×2 array of disk amplifiers sharing common flash lamps. Originally conceived by Lawrence Livermore National Laboratory (LLNL) as a concept for the ATHENA multimegajoule laser system and designed by LLE personnel with the support and collaboration of LLNL, the MSA was successfully constructed and met or exceeded its design goals. The MSA serves as a proof-of-concept of arrayed amplifiers for future Laboratory Microfusion Facility (LMF) consideration, and was an important first step in the development of disk amplifiers for the OMEGA Upgrade.

Section 1
PROGRESS IN LASER FUSION

1.A Saturation and Power Balance in Multibeam Lasers for Laser Fusion

Introduction: Irradiation Uniformity Considerations for Laser Fusion
Successful demonstration of laser-fusion feasibility is critically dependent on the ability to drive the implosion with a very high degree of symmetry over the whole time of the target irradiation. For direct-drive laser fusion, this implies an irradiation uniformity over the entire surface of the target, which should not deviate from perfect uniformity by more than $\approx 1\%$ rms at any time.[1] Such uniformity can only be realistically achieved with a fairly large number of incident laser beams symmetrically disposed around the target.[2] At the same time each of these beams must have a reproducible on-target beam intensity distribution that must be the same for all beams and should also be as smooth as possible.[3] (The exact definition of smoothness, including temporal variations of any microstructure in the intensity distribution, is under investigation at present and will not be discussed further in this section.) To maintain a high degree of irradiation uniformity over the entire laser-pulse duration, equal power in each of the beams is required at any time, hence the term "power balance." If all beams are power balanced then all beam energies are the same. Since experimentally it is much easier to measure laser-pulse energy than instantaneous power in each beam, energy balance has been recognized to be essential for laser fusion. Power balance is obtained as a consequence of energy balance if all beamlines are identical. However, typical high-power beamlines are not identical, the consequences of which are the subject of the present study.

The study was stimulated by recent efforts at LLE to achieve high densities in direct-drive laser-fusion experiments with neutron yields

comparable to those predicted by one-dimensional hydrodynamic code simulations.[4] These experiments have led to an investigation of all aspects of irradiation uniformity and prompted many measurements relating input and output temporal pulse shapes, energy balance, and gains and losses in the 24 beamlines of OMEGA–a frequency-tripled Nd:glass laser system.[5,6,7] All nonlinear effects on a laser beam along its path from oscillator to target are potential contributors to power imbalance (linear effects are easily compensated for by attenuators or simple redistribution of energy among beamlines). The primary nonlinear effects include gain saturation in the laser amplifiers and harmonic frequency conversion at the output. In the following sections these two effects will be treated separately: first, the generic problem of amplifier saturation, which affects essentially all large, efficiently designed laser systems; second, the effects of harmonic conversion, which apply only to lasers with harmonic converters at their output.

Saturation in Laser Amplifiers

Saturation in laser amplifiers is well understood[8] and is due to energy extraction from the active medium. Trenholme[9] has shown how Gaussian temporal pulses are distorted if a single saturated amplifier is considered, or if the main saturation effects only occur in the final laser amplifier. The distortion of more complex shaped pulses was treated for the OMEGA laser system some time ago;[10] however, the situation becomes considerably more complicated if we consider modern, more efficient laser designs with many beams.[11] In such lasers an attempt is made to extract as much energy as possible from each amplifier stage without incurring damage or other deleterious effects. This leads to distributed saturation effects whose total temporal pulse distortion far exceeds that predicted for a saturated final amplifier only. On the other hand, the problem still maintains Trenholme's essential conclusion that the ratio of the output fluence to the saturated fluence (F_{out}/F_{sat}) is the most important parameter. For the case of distributed saturation, the saturation pulse distortion depends on F_{out}/F_{sat} in each of the amplifier stages where this ratio exceeds a value of $F_{out}/F_{sat} \gtrsim 0.1$.

The small-signal gain G_o of an active medium is observed experimentally only if the output fluence is small compared to the saturation fluence; otherwise, the output fluence of a loss-less amplifier is given by the Frantz-Nodvik equation[12]

$$F_{out} / F_{sat} = \ell n \left\{1 + G_o \left[\exp\left(F_{in} / F_{sat} - 1\right)\right]\right\} , \quad (1)$$

where F_{in} is the input fluence to the amplifier. The small-signal gain can also be written as $G_o = \exp(E_{st}\, \ell / F_{sat}) = \exp(F_{st}/F_{sat})$, where E_{st} is the stored energy in J/cm^3, ℓ is the length of the amplifier, and F_{st} is a stored fluence in J/cm^2, i.e., the stored energy per unit area. Since all fluences appear only as ratios relative to F_{sat}, all conclusions relating to saturated amplification are therefore generic for any laser system.

No information on temporal pulse-shape distortions can be obtained from Eq. (1). However, if we divide the incident pulse into small temporal segments and the amplifier into small spatial segments, we can propagate each temporal segment through the amplifier and follow the temporal evolution of the entire pulse as it passes through the amplifier, provided we

reduce the stored energy in each spatial segment by the energy extracted by each temporal segment as it is amplified. We have written a simple code that calculates this pulse distortion for any number of amplifiers including losses, beam expanders, and beam splitters. Within each spatial segment these calculations use the small-signal gain for this segment as the fluences per temporal interval are sufficiently small.

The most obvious manifestation of saturation distortion of Gaussian laser pulses is the shift of the pulse maxima toward earlier times as evident in Fig. 41.1. The figure shows the output pulse shape for the 60-kJ design output energy at the fundamental laser wavelength of $\lambda_L = 1.054\ \mu m$ for the planned 60-beam OMEGA Upgrade Nd:glass laser, whose proposed staging diagram is shown in Fig. 41.2. For this case the output fluence just after the final amplifier is $1.25 \times F_{sat}$. The abscissa of Fig. 41.1 was chosen in terms of half-widths of the laser pulse since the pulse distortion is independent of the actual pulse duration for 0.5-ns to 10-ns pulses,[13] the typical range of interest for fusion lasers. The saturation distortion becomes more important as the laser is designed to be more efficient, i.e., as the output fluences in the intermediate and final amplifiers approach or exceed the saturation fluence. This is easily seen in the dotted pulse shape in Fig. 41.1, which is obtained if a hypothetical amplifier is assumed whose small-signal gain equals the combined gain of all the amplifiers in Fig. 41.2 and without intermediate losses, beam splitters, or magnifying spatial filters. Clearly the pulse distortion is much reduced in this case but such a laser would be very inefficient and cost prohibitive.

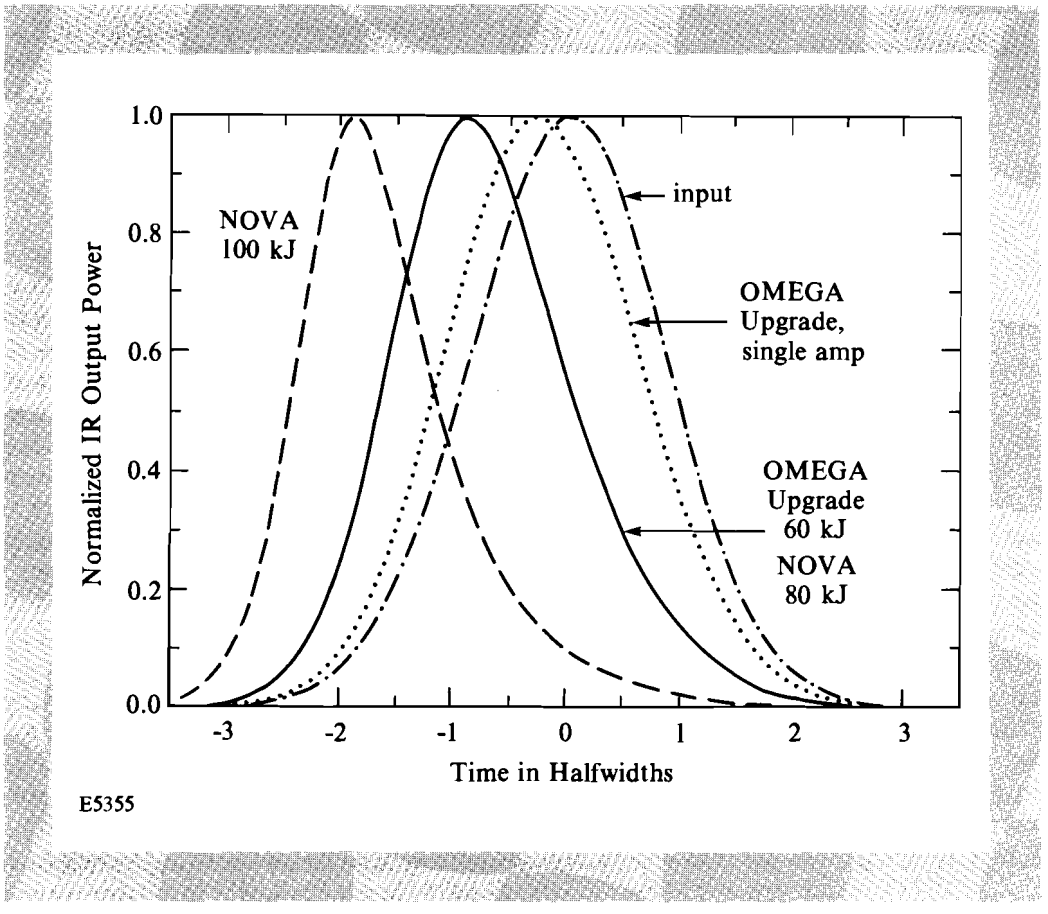

Fig. 41.1
Distortion of Gaussian input pulses in large laser chains.

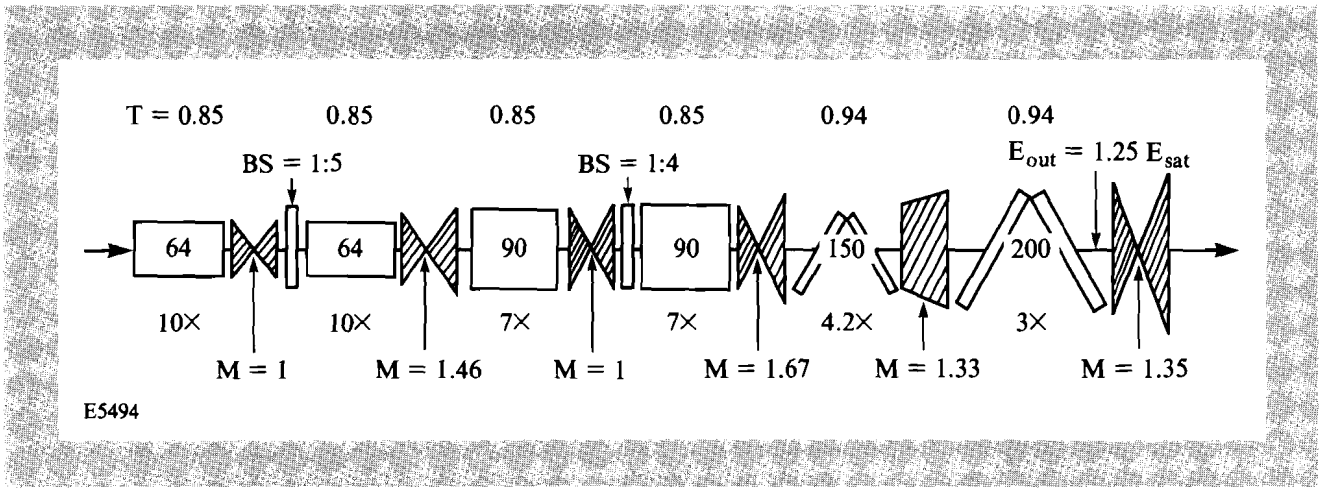

Fig. 41.2
Staging diagram for the proposed OMEGA Upgrade laser. Nominal sizes are shown inside each amplifier; small-signal gains are shown below each amplifier; typical transmission losses and beam-splitting ratios are shown above the amplifiers.

It is interesting to compare the pulse-shape distortion calculated for the OMEGA Upgrade with that expected for the NOVA laser system at the Lawrence Livermore National Laboratory.[11] At the 80-kJ output level the pulse-shape distortion is practically indistinguishable from that for the 60-kJ OMEGA Upgrade design (solid line in Fig. 41.1). This is surprising in light of the completely different amplifier staging for the two laser systems. However, the pulse distortion for NOVA at 100-kJ output is dramatically higher (left-most curve in Fig. 41.1); for the recently demonstrated 120-kJ output capability of NOVA the output pulse shifts practically out of the range plotted in Fig. 41.1.

Power Balance in Multibeam Laser Systems

If a large number of beams are incident on the target with the requirement of continued instantaneous near-perfect irradiation uniformity, we must have equal powers, i.e., equal pulse shapes, in all irradiating laser beams. Since laser-pulse distortion increases with laser efficiency we can expect a concomitant increase in sensitivity of the temporal pulse shapes of the various beams to small fluctuations in individual beam energies. These energies can typically be measured with an accuracy of ≤1% and, under optimum conditions, rms beam-energy-balance values of 1% to 2% have been achieved.[14,15] However, the corresponding peak-to-valley excursions in beam energies are typically 3 to 4 times larger. Therefore, it is important to know the consequences of such energy imbalances on the power balance between individual beams.

Figure 41.3 shows the calculated, temporally dependent power imbalance $\Delta P/P_{av}$ for pairs of beams whose energies differ by 5% and for the same laser configurations, output fluences, and output energies as shown in Fig. 41.1. We notice that the 5% beam-energy imbalance at the output of the laser chain translates into ≤18% power imbalance at early times of the originally Gaussian laser pulse for the OMEGA Upgrade design specifications. For the 100-kJ NOVA output the power imbalance is considerably worse, while the

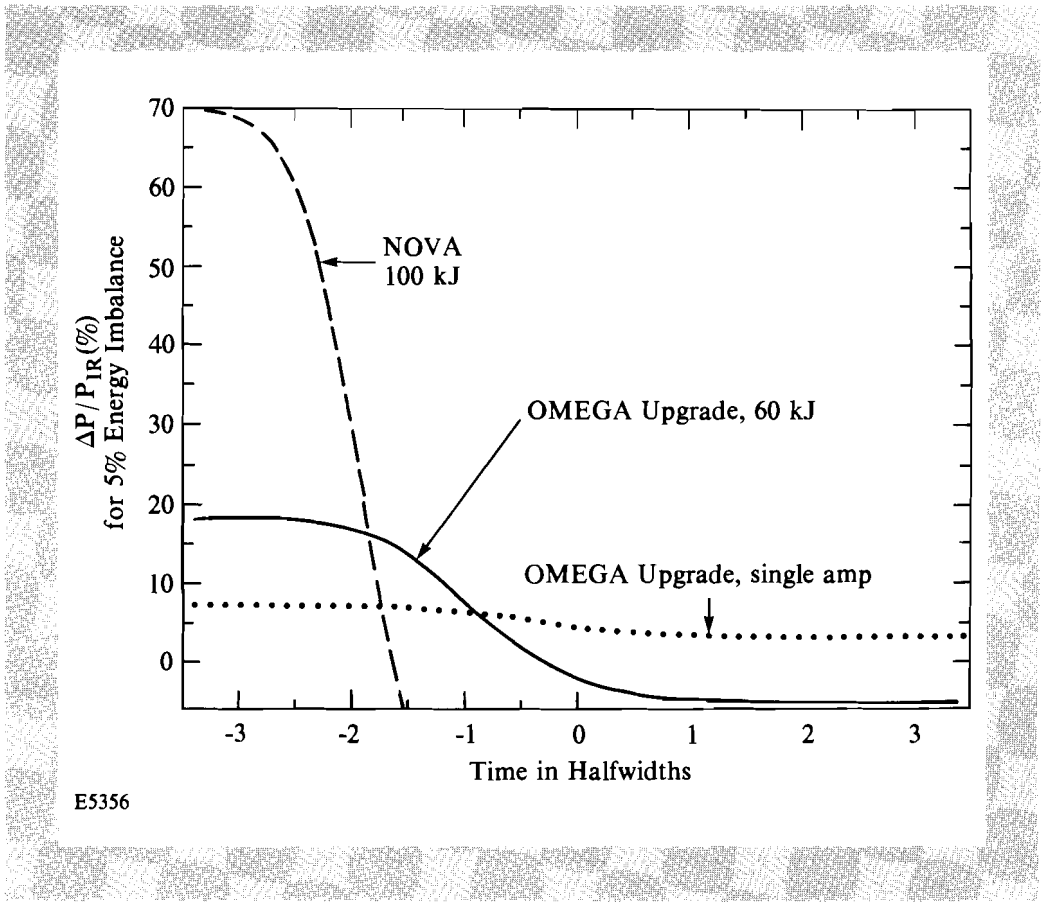

Fig. 41.3
Temporal dependence of the IR power balance between two beamlines of the proposed OMEGA Upgrade (University of Rochester) and NOVA (Lawrence Livermore National Laboratory) laser systems for two beamlines whose output energies differ by 5%.

curve for 80-kJ NOVA is indistinguishable from that for the OMEGA Upgrade at full design value. We note that at $\approx 2\%$ of the peak output power the power imbalance is still approximately 95% of its asymptotic early-time value in all cases.

The curves in Fig. 41.3 were calculated for identical gains and losses in the laser chain under the assumption that the only contributor to the energy imbalance was the input energy to the amplifier chain. This, however, is only one possible scenario leading to power imbalance due to amplifier saturation. Alternative sources for power imbalance include differing gains and/or losses along the laser chain. To assess their relative importance we assume perfect energy balance but differing gains (losses) in the two beams whose temporal power imbalance $\Delta P/P_{av}$ is to be evaluated. In addition, we can also assume compensating small-signal gains and losses in each stage such that the net small-single stage gain remains unchanged. We have further assumed that any changes in gains or losses are made in the same sense (increasing or decreasing) in all stages of one beamline.

The power imbalances due to energy imbalance, gain imbalance, loss imbalance, and compensated gain-loss imbalances are shown in Fig. 41.4 for the nominal 60-kJ OMEGA Upgrade design. The abscissa of this graph represents the relative changes in the variables under consideration ($\Delta E/E$, $\Delta G/G$, etc.). A value of $\Delta G/G$ (or $\Delta T/T$) = 5% implies that the small-signal gain [or transmission = 1 – (loss)] of each amplifier stage in one of the two beams was increased by 5%. Thus, for the staging diagram of Fig. 41.2 with six amplifier stages, a 5% change in stage gain corresponds to ≈30% change in total small-signal system gain. While this may appear to be a large gain imbalance, actual gain variations between beams in large laser systems can easily exceed such values.

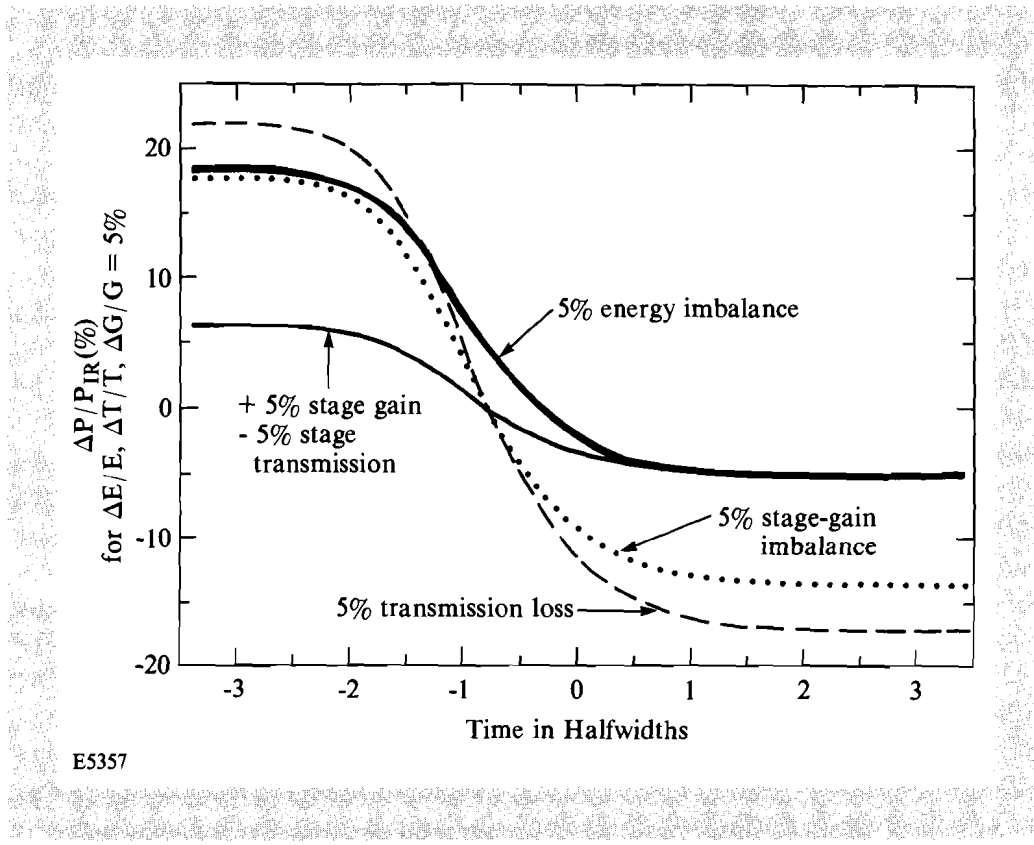

Fig. 41.4
Temporal dependence of the IR power imbalance between two beamlines of the OMEGA Upgrade at nominal 60-kJ output with a Gaussian temporal pulse as shown in Fig. 41.1. The different curves relate to power imbalance due to 5% energy imbalance between the two beams (heavy solid line), 5% per stage gain imbalance (dotted line), 5% per stage loss imbalance (dashed line), and compensated 5% gain and loss balance per stage ($\Delta G/G = -\Delta T / T = 5\%$, thin solid line).

Perfect energy balance but unequal gains or losses in two different beams can lead to very pronounced power imbalance, as shown in Fig. 41.4. Significantly lower power imbalance is observed if the losses and gains are balanced in each stage such that the product of gain and transmission is constant. In other words, we may increase the gain in each stage by 5% without degrading the power balance unduly, provided we increase the

losses (decrease the transmission T) in each stage correspondingly. This result is intuitively obvious and the calculations bear this out very clearly (see the thin solid curve in Fig. 41.4).

The implications of Fig. 41.4 are several-fold: Power balance requires energy balance plus detailed gain and loss balance throughout the laser system. The exact requirements for energy, gain, and loss balance depend strongly on the detailed laser design; in particular, as the laser design becomes more efficient, i.e., as the fluence levels approach or exceed the saturation fluence, the demands on energy, gain, loss, and detailed interstage gain-loss balance become significantly more stringent and harder to meet.

Power Balance and Harmonic Conversion

Over the past ten years, laser-fusion research has shown that irradiation wavelengths of ≤ 0.5 μm are required to achieve acceptable target performance. For lasers with longer fundamental wavelengths, this requirement implies harmonic conversion of the laser output; however, the inherently nonlinear nature of harmonic frequency conversion is a source of great concern for power balance.

We now turn to the problems associated with third-harmonic conversion of 1-μm glass lasers for which the relevant third-harmonic energy-conversion curve is shown in Fig. 41.5. Also shown in this figure are the conversion curves for angle- and polarization-detuned crystals[6] as well as experimental data obtained on the 24-beam OMEGA laser facility. The narrow cross-hatched area close to the theoretical optimum crystal performance includes the rms performance of all 24 conversion-crystal cells for over 70 OMEGA target shots. The worst-performing conversion cells for the same set of shots have conversion efficiencies that lie within the larger cross-hatched band labeled "p-v" (peak-to-valley). We note that in an rms sense all data indicate crystal-tuning capability within ≤50 μrad, with the worst performers exceeding 100 μrad by a small amount. Since these measurements were taken, mechanical improvements have been made to the cell mounts that should further reduce these error bars; however, we have not yet collected a sufficiently large new data base to quantify the improvements.

Detuned conversion crystals rapidly lead to pulse-shape distortions and concomitant increases in power imbalance as discussed in Ref. 16. However, even perfectly tuned crystal converters significantly aggravate any IR power-balance problems incident on them (see Fig. 41.6). This figure is analogous to Fig. 41.4 but includes third-harmonic conversion for perfectly tuned crystals. Note that the 18% IR power imbalance generated by a 5% IR energy imbalance for the nominal OMEGA Upgrade output results in a >50% power imbalance at the third-harmonic output. The corresponding third-harmonic power at that time is $\approx 10^{-3}$ of the peak power, i.e., at a time when relatively little plasma surrounds the laser-fusion target and no significant thermal smoothing is expected.

Power imbalance as a result of different gains or losses in the individual amplification stages of the two beamlines also leads to much higher power

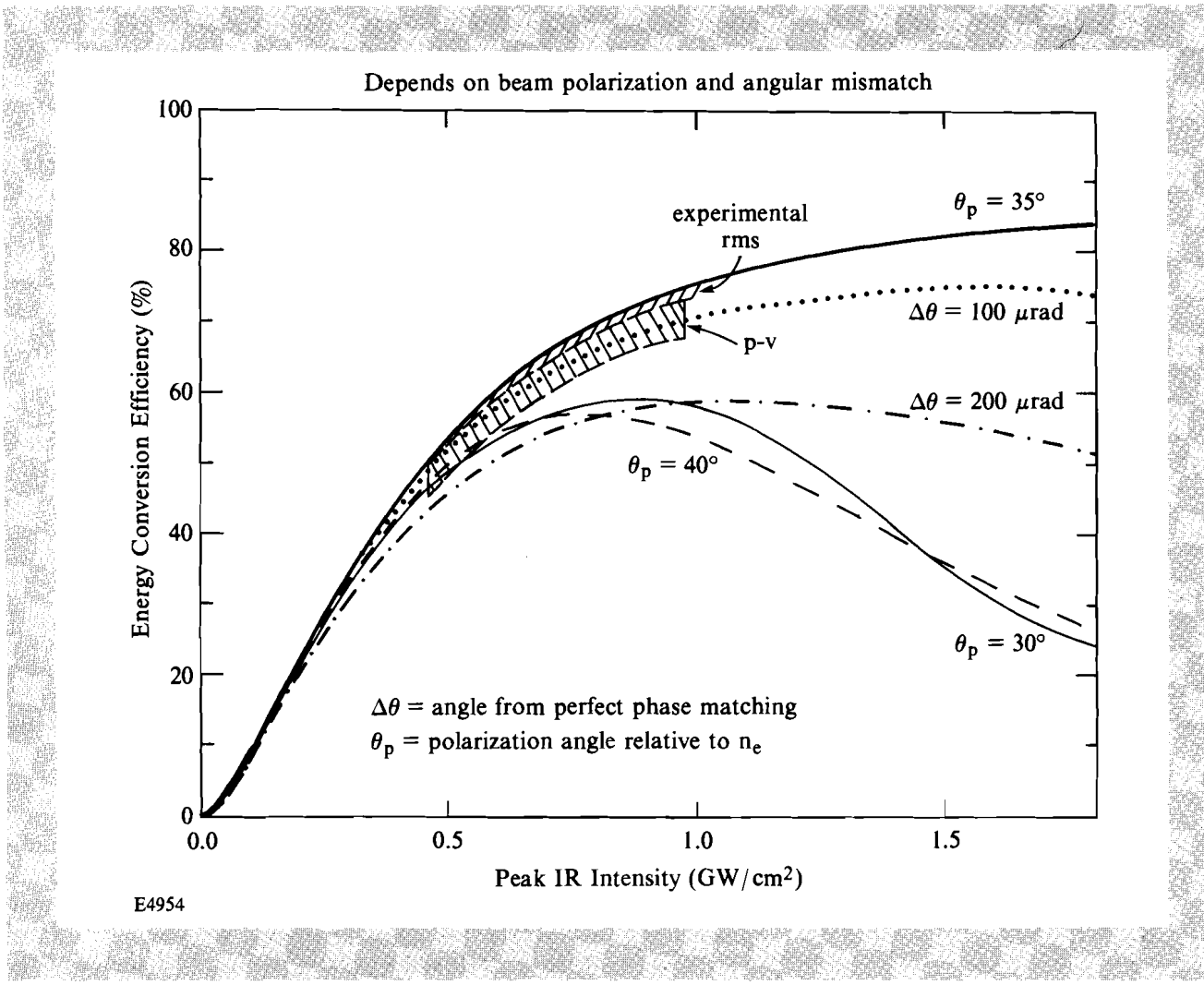

Fig. 41.5
Third-harmonic energy-conversion curves for various angular- and polarization-tuning conditions. Also shown is the range of average 24-beam OMEGA conversion performance (narrow cross-hatched band labeled "experimental rms") and the maximum deviation from perfect tuning (wide cross-hatched band labeled "p-v") taken from over 70 on-target laser system shots.

imbalance in the third harmonic than at the fundamental laser wavelength (compare Figs. 41.4 and 41.6). Balancing gains and losses in the individual amplification stages reduces these effects to manageable levels, as observed for the IR in Fig. 41.4.

In Fig. 41.7 we have summarized the effects of power balance as a result of energy imbalance, gain imbalance, and loss imbalance at 10^{-3} of the peak of the third-harmonic output. If we postulate a maximum-permissible power imbalance of, for example, 20% at any time between any two beams, then we can use Fig. 41.7 to estimate the tolerances on energy balance to be $\leq 2.5\%$, while 6% differences in losses or gains per stage could be acceptable provided they are compensated for, giving equal small-signal gain per stage in the two beamlines. Since these calculations assume that all gains or losses

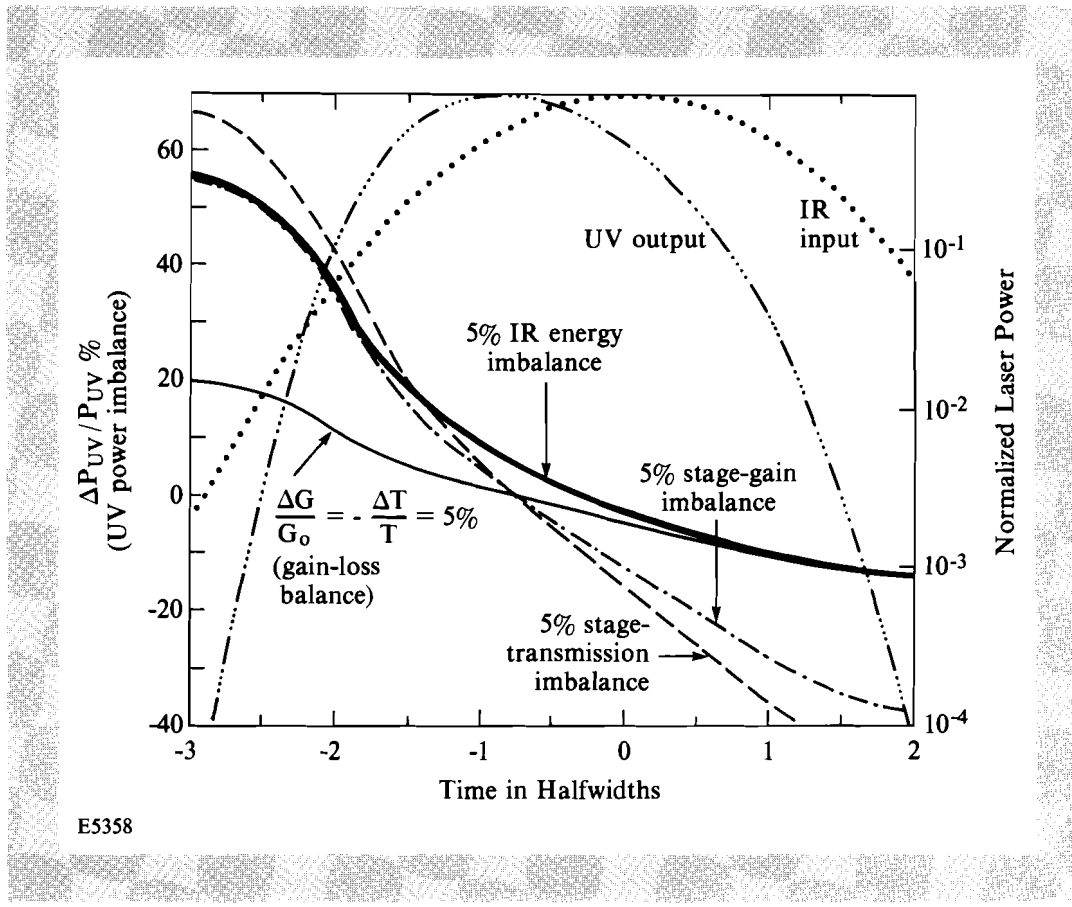

Fig. 41.6
Temporal dependence of the UV power balance between two beams of the OMEGA Upgrade at 60-kJ nominal IR output. The heavy solid line is the power balance due to a 5% IR output-energy imbalance; the dashed and dashed-dotted lines are due to 5% transmission (loss) and gain imbalance per stage at perfect IR output-energy balance; and the light solid line corresponds to 5% compensated gains and losses per stage and equal-output beam energies ($\Delta G/G = -\Delta T / T = 5\%$).

per stage of one beam would be increased (or decreased), these results certainly represent a somewhat pessimistic view. On the other hand, achieving even 10% variation in small-signal gains among the equivalent amplification stages of different beamlines represents a challenge in real lasers.

Conclusions

High-compression inertial fusion targets demand a high degree of power balance for all the beams incident on the target. Power balance implies equal pulse shapes and energies in all the beams, placing severe conditions on all nonlinear elements of the laser system such as amplifiers and harmonic frequency converters. We have shown that energy-balance requirements become demanding ($\leq 2\%$ between any two beams) if power balance in the third harmonic output is to stay below $\approx 20\%$ between that pair of beams at any time during the pulse. This condition was derived for laser systems whose beamlines are all identical. If equivalent amplification stages in

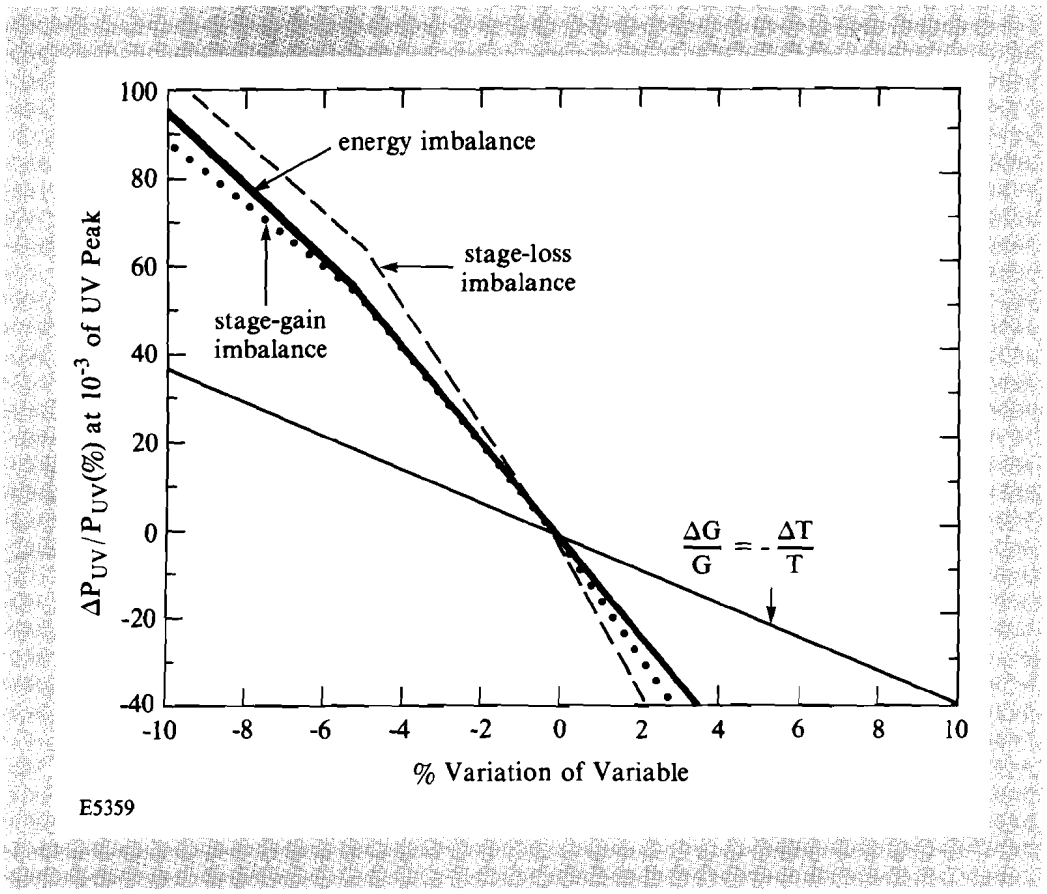

Fig. 41.7
UV power imbalance between two OMEGA Upgrade beamlines at early time when the power has reached 10^{-3} of its peak. The heavy line corresponds to energy imbalance but otherwise identical beams; the other lines correspond to perfect energy balance but different gain or loss imbalance (dotted and dashed curves) and compensated gains and losses per stage ($\Delta G/G = -\Delta T / T$, light solid line).

different beamlines differ in their gains or losses, a very pronounced power imbalance may result even in the presence of perfect energy balance. This detrimental effect is mitigated by balancing the gains and losses in equivalent amplification stages to yield the same net small-signal gain. All these power-balance problems are most noticeable in the early part of the laser pulse rather than near its peak.

In summary, power-balance considerations must form an integral part of any modern design for a laser-fusion facility, and they may significantly impact the staging of the laser system and its efficiency.

ACKNOWLEDGMENT

This work was supported by the U.S. Department of Energy Division of Inertial Fusion under agreement No. DE-FC03-85DP40200 and by the Laser Fusion Feasibility Project at the Laboratory for Laser Energetics, which has the following sponsors: Empire State Electric Energy Research Corporation, New York State Energy Research and Development Authority, Ontario Hydro, and the University of Rochester.

REFERENCES

1. LLE 1989 Annual Report, p. 2 [or LLE Review **37**, 2 (1989)].
2. B. Badger *et al.*, LLE Internal Report #152 (1984); S. Skupsky and K. Lee, *J. Appl. Phys.* **54**, 3662 (1983).
3. S. Skupsky, R. W. Short, T. Kessler, R. S. Craxton, S. Letzring, and J. M. Soures, *J. Appl. Phys.* **66**, 3456 (1989); LLE Review **33**, 1 (1987).

4. F. J. Marshall, S. A. Letzring, C. P. Verdon, S. Skupsky, R. L. Keck, J. P. Knauer, R. L. Kremens, D. K. Bradley, T. Kessler, J. Delettrez, H. Kim, J. M. Soures, and R. L. McCrory, *Phys. Rev. A* **40**, 2547 (1989); R. L. McCrory, J. M. Soures, C. Verdon, M. Richardson, P. Audebert, D. Bradley, J. Delettrez, L. Goldman, R. Hutchison, S. Jacobs, P. Jaanimagi, R. Keck, H. Kim, T. Kessler, J. Knauer, T. Kremens, S. Letzring, F. Marshall, P. McKenty, W. Seka, S. Skupsky, and B. Yaakobi, *Laser Interaction and Related Plasma Phenomena*, Vol. 8, edited by H. Hora and G. H. Miley (Plenum Press, New York and London, 1988), p. 483.

5. J. Bunkenberg, J. Boles, D. C. Brown, J. Eastman, J. Hoose, R. Hopkins, L. Iwan, S. D. Jacobs, J. H. Kelly, S. Kumpan, S. Letzring, D. Lonobile, L. D. Lund, G. Mourou, S. Refermat, W. Seka, J. M. Soures, and K. Walsh, *IEEE J. Quantum Electron.* **QE-17**, 1620 (1981).

6. R. S. Craxton, *Opt. Commun.* **34**, 474 (1980); W. Seka, S. D. Jacobs, J. E. Rizzo, R. Boni, and R. S. Craxton, *Opt. Commun.* **34**, 469 (1980).

7. W. Seka, J. M. Soures, S. D. Jacobs, L. D. Lund, and R. S. Craxton, *IEEE J. Quantum Electron.* **QE-17**, 1689 (1981); J. M. Soures, R. L. McCrory, K. A. Cerqua, R. S. Craxton, R. Hutchison, S. D. Jacobs, T. Kessler, J. Kelly, G. Mourou, W. Seka, and D. Strickland, *Laser Research and Development in the Northeast* (SPIE, Bellingham, WA, 1987), Vol. 709, p. 74.

8. A. E. Siegman, *LASERS*, Chap. 10 (University Science Books, Mill Valley, CA, 1986), p. 362.

9. J. B. Trenholme and K. R. Manes, Lawrence Livermore National Laboratory Report UCRL-51413 (1972); Lawrence Livermore National Laboratory Report UCRL-52868 (1980).

10. W. Friedman, W. Seka, and J. M. Soures, *Opt. Commun.* **25**, 103 (1978).

11. J. T. Hunt and D. R. Speck, *Opt. Eng.* **28**, 461 (1989).

12. L. M. Frantz and J. S. Nodvik, *J. Appl. Phys.* **14**, 2346 (1975).

13. W. E. Martin and D. Milam, *IEEE J. Quantum Electron.* **QE-18**, 1155 (1982).

14. K. Nishihara and S. Nakai, to appear in *Laser Interaction and Related Plasma Phenomena*, edited by H. Hora and G. H. Miley (Plenum Press, New York and London, 1990).

15. J. P. Knauer, R. L. McCrory, J. M. Soures, C. P. Verdon, F. J. Marshall, S. A. Letzring, S. Skupsky, R. L. Kremens, H. Kim, R. Short, T. Kessler, R. S. Craxton, J. Delettrez, R. L. Keck, and D. K. Bradley, to appear in *Laser Interaction and Related Plasma Phenomena*, edited by H. Hora and G. H. Miley (Plenum Press, New York and London, 1990).

16. LLE Review **37**, 16 (1988).

1.B Numerical Modeling of Effects of Power Balance on Irradiation Nonuniformities

The need for good irradiation uniformity in inertial-confinement-fusion (ICF) target implosions has been well understood for some time.[1-6] In order to ignite and sustain thermonuclear burn, an ICF target must be symmetrically driven to very high densities [> 1000 times the liquid density of DT fuel (XLD)] while generating ignition temperatures (>5 keV).[7] The success of such implosion dynamics is dependent on the drive uniformity of the ablation front within the target. Perturbations at the ablation front are determined by the uniformity of the absorbed laser energy arriving from the critical surface. Although nonuniformities in this energy are smoothed in transit between the corona and the ablation surface,[1] the effect of any surviving nonuniformities is to perturb the hydrodynamic motion of the ablation front that can, in turn, serve to seed the possible secular and/or Rayleigh-Taylor unstable growth of this surface. Clearly, only very good irradiation uniformity can control these factors.

Laser irradiation nonuniformities can arise from several sources, including beam mispointing, energy and power imbalance, beam overlap due to the system geometry, and the individual profiles of the laser beams.[3] Over the past two years, it has become increasingly evident at LLE that improper power balance among the 24 OMEGA laser beams and poor laser-beam profiles have led to severe degradation of target performance when compared to one-dimensional predictions.[8] In attempting to model these nonuniformities it has been found useful to apply a spherical-harmonic decomposition of the applied radiation, since the effect on target performance is different for the long and short spatial wavelengths of nonuniformity.[6]

Calculations[3] (Table 41.I) have shown that power imbalance contributes to the long-wavelength structure ($\ell \lesssim 8$) while nonuniformities in the individual laser-beam profiles contribute primarily to the short-wavelength structure ($\ell \gtrsim 8$). Although there are mode-mode interactions between the two groups during an implosion, it is possible to evaluate the effects of each group separately. Significant effort has been exercised in analyzing and correcting the laser-beam profiles and is discussed in Refs. 9–13. This article will deal with evaluating the time-dependent sources of power imbalance that contribute to the long-wavelength perturbations.

The term "power balance" can be applied to a wide range of temporal, beam-to-beam intensity differences arising from laser amplifier saturation, variations in frequency conversion (detuning, polarization rotation, etc.), and/or the transport of energy from the conversion crystals to the target. Modeling the effects of these factors has required adapting our uniformity codes to treat time-dependent density and temperature profiles, as well as to include numerical models to simulate the individual power-imbalance contributions. Such an analysis will show that our efforts to control the tuning of the frequency-conversion crystals and the careful characterization of the UV transport losses have significantly reduced their contributions to

Table 41.I: Summary of the contributions of irradiation-nonuniformity sources to the various Legendre modes in ICF targets.

Modes	Source
$\ell = 1-4$	• pointing error • energy and power imbalance
$\ell = 8-12$	• beam overlap (24 –32 beams)
$\ell \gtrsim 8$	• beam imperfections

TC2780

the overall nonuniformity. However, effort still needs to be applied to characterize and correct misshaped pulses that can lead to very significant increases (factor of 3 to 5) in irradiation nonuniformity very early in the implosion.

We have divided this article into four sections: first, a discussion of the overall numerical method used to ascertain the nonuniformities; second, the individual contributions to power imbalance and illustrations of how they are modeled; third, numerical results showing how each of the power-imbalance terms affect the level of nonuniformity; and fourth, an experiment using the OMEGA laser system in which deliberate levels of power imbalance were applied. We also present a comparison of the experimental data with a simulation using the two-dimensional hydrodynamics code *ORCHID*.

Numerical Method

Several investigators have examined the uniformity produced by overlapping multiple laser beams on spherical targets.[1,3,14–17] Research at LLE has emphasized the decomposition of the laser energy in terms of spherical harmonics to obtain information about the spatial wavelengths of the nonuniformity on target for a given beam-overlap pattern.[3] The illumination pattern on target can be expressed as the product of two factors: (1) a "single-beam" factor that depends on the focal position, f-number of the lens, assumed target conditions, energy and possible temporal imbalance among individual beams (power balance), and the individual beam profiles; and (2) a "geometric" factor that is determined by the number and orientation of the individual beams about the target.

The method presented in this article is an adaptation of this previous work. It differs from that work in three main areas: First, instead of using an analytic, isothermal density profile, we use the one-dimensional hydrodynamics code *LILAC*[18] to provide time-dependent temperature and density profiles of the laser-absorption region. Second, our method considers the contribution of energy deposited between the critical surface and the surface determined by the position of the local peak in the electron temperature. The previous study considered only energy deposited between the critical and quarter-critical density surfaces. Finally, a full spherical-harmonic

decomposition of the absorbed energy is performed, allowing for the full phase information of the applied perturbation to be retained.

The actual calculation of the nonuniformity level starts by using *LILAC* to determine the temporal profiles of temperature and density, as opposed to previous treatments that assumed an analytical fit to the density profile under isothermal conditions. A two-dimensional geometrical optics ray-trace routine, taken from *ORCHID*, is employed to determine the azimuthally symmetric absorbed-energy profile due to a single beam. Several beam profiles, including patterns with time-dependent smoothing, can be considered. An angular source function is determined by collapsing (projecting) the absorbed energy to a single surface. This angular source function is then resolved into a series of Legendre polynomials.

Several prescriptions for collapsing the absorbed energy have been considered. Originally, only the energy between the critical and quarter-critical density surfaces (i.e., "quarter-critical cutoff") was considered to contribute to the intensity pattern.[3] However, since significant amounts of energy are deposited at densities less than quarter critical as an implosion proceeds, we believe that this cutoff is too restrictive and may have led to predictions of excessive nonuniformity levels. Other work[19] has shown that it is possible to weigh energy contributions from the entire corona as a function of density. However, the coefficients in such analytic formulations have to be recalculated several times during the implosion. Coefficients that yield good results early in the implosion become too optimistic at late times by allowing contributions from absorbed energy that cannot participate in the ablation process. A compromise has been found by examining the density and the electron-temperature profiles for a typical ICF implosion. It was found that there exists a maximum in the electron temperature outside of the quarter-critical density surface. Since thermal conduction is dominated by electron transport, it can be argued that only the energy at or within this temperature maximum will flow into the ablation region. Energy outside this region will flow out into the expanding corona and, as such, will not participate directly in determining the drive uniformity. Using the electron-temperature maximum cutoff, the absorbed energy between the critical surface and the cutoff is collapsed by radial integration to a single surface and a Legendre decomposition is applied to resolve the angular-source function into a single-beam series. A full mapping can then be made for the entire system of beams considered using this single-beam series.

The angle between each beam and a mapping location on the sphere is determined by the angle equation for two vectors on the unit sphere

$$\cos\gamma = \cos\theta\cos\theta' + \sin\theta\sin\theta'\cos(\varphi - \varphi'),$$

where θ and φ represent the coordinates of the laser beam and θ' and φ' are the coordinates of the mapping location. The single-beam series is evaluated for this angle to determine the intensity contribution of each laser beam to that location. The contribution of each beam can then be altered by a beam-balance factor due to the effects of power imbalance. How these factors are determined is discussed in the next section.

The procedure above is repeated for all beams over the sphere until a full spherical mapping is obtained. (Eventually we shall incorporate a full three-dimensional ray-trace routine to evaluate more realistic beam profiles. How such information might be incorporated into a two-dimensional hydrodynamics simulation is discussed later.) The mapping is now decomposed in spherical harmonics using a Laplace series involving the real functions $Y^e_{\ell m}$ and $Y^o_{\ell m}$,[20]

$$Y^e_{\ell m}(\hat{\Omega}) = P^m_\ell(\cos\theta)\cos m\varphi$$

$$Y^o_{\ell m}(\hat{\Omega}) = P^m_\ell(\cos\theta)\sin m\varphi$$

with

$$P^m_\ell(x) = \frac{1}{2^\ell \ell!}\left(1-x^2\right)^{m/2}\frac{d^{m+\ell}}{dx^{m+\ell}}\left(x^2-1\right)^\ell \qquad -\ell \le m \le \ell.$$

The intensity mapping $f(\hat{\Omega},t)$ can be expanded in these spherical harmonics as

$$f\left(\hat{\Omega},t\right) = \sum_{\ell}^{\infty}\sum_{m=0}^{\ell}\left[a_{\ell m}(t)Y^e_{\ell m}\left(\hat{\Omega}\right) + b_{\ell m}(t)Y^o_{\ell m}\left(\hat{\Omega}\right)\right]$$

where

$$a_{\ell m}(t) = \int d\hat{\Omega}\, f(\hat{\Omega},t)\, Y^e_{\ell m}(\hat{\Omega})$$

$$b_{\ell m}(t) = \int d\hat{\Omega}\, f(\hat{\Omega},t)\, Y^o_{\ell m}(\hat{\Omega})\ .$$

The traditional measure of the irradiation nonuniformity is the rms deviation defined as

$$\sigma_{\text{rms}}(t) = \left\{\frac{1}{4\pi}\int d\hat{\Omega}\left[f(\hat{\Omega},t) - f_0(t)\right]^2\right\}^{1/2}.$$

Performing the subtraction and employing orthogonality, this becomes

$$\sigma_{\text{rms}}(t) = \left\{\frac{1}{4\pi}\sum_{\ell=1}^{\infty}\sum_{m=0}^{\ell}\left[a^2_{\ell m}(t) + b^2_{\ell m}(t)\right]\right\}^{1/2}.$$

Since at present we do not have a three-dimensional hydrodynamics code available to simulate the full phase perturbations derived from such a decomposition, the phase information between the various modes is simply

summed together. This is accomplished by summing over the density of states

$$\alpha_\ell(t) = \sqrt{\frac{1}{4\pi}\sum_{m=0}^{\ell}\left[a_{\ell m}^2(t) + b_{\ell m}^2(t)\right]}.$$

The rms deviation of the nonuniformities is then given by

$$\sigma_{\text{rms}}(t) = \sqrt{\sum_{\ell=1}^{\infty}\alpha_\ell^2(t)}\ .$$

Since the growth of a particular ℓ-mode is degenerate with respect to all of its m-modes (i.e., the pure $m = 0$ harmonic grows the same regardless of its orientation on the sphere), the use of the α_ℓ terms works well when one is comparing the merits of one illumination scheme to another, or calculating the Rayleigh-Taylor growth of these modes throughout the implosion. However, one cannot use several α_ℓ terms directly in two-dimensional simulations because the phase orientations of the different azimuthally symmetric modes do not typically share the same vector on the unit sphere. (One could isolate a particular ℓ-mode on target through an appropriate choice of coordinates and have all of the $m \neq 0$ modes vanish. This would then represent a pure, azimuthally symmetric harmonic. It would then be possible to simulate the effects of this mode throughout the implosion using *ORCHID*. An experiment designed along these lines was performed and the results are presented later in this section.)

Modeling Power Imbalance

The effects of power imbalance are modeled by changing the deposition pattern of each beam by a beam-balance factor. While some sources of power imbalance are static, such as the reduced transmission in a turning mirror, most sources are time dependent and are related to beam misshaping and intensity mismatching. The beam-balance factor must therefore be calculated at each time step throughout the implosion. The modeling of each mechanism is now discussed.

Amplifier Saturation

Gain saturation in laser amplifiers results in changes to the shapes of individual pulses. We model these distorted pulses in two ways. The first method assumes all pulses are initially perfectly timed, equal-power Gaussians. Random analytic variations can then be applied to affect the arrival time, full width at half maximum (FWHM), and peak power of each of the individual pulses. This method, while not considering the effect of non-Gaussian pulse shapes, does provide the ability to consider a wide range of pulse distortions.

Recently, as described in article 1.A, it has become possible to evaluate some aspects of gain saturation, though it is still very difficult to determine experimentally the actual difference among all of the pulses, or the exact shape of an individual pulse.[21,22] However, it is now possible to determine a temporal power-ratio history between two of the separate infrared (IR) pulses. The power in each of the remaining beams is then assumed to lie in the envelope determined by this single beam-beam pair throughout the implosion. An important aspect of this method is that it does not restrict the

pulse shapes to be Gaussian. As these power histories become available for individual experiments, it will be possible to model each implosion with the correct amount of power imbalance due to gain saturation in the amplifiers.

Frequency-Conversion Crystal Detuning

The role of the frequency-conversion crystals in contributing to the total power imbalance in the laser system is due to their nonlinear response to the input laser intensity, as shown in Fig. 41.8. This response can vary significantly as a function of both the polarization angle of the input laser light and the amount of physical detuning of the tripler crystal from its optimum angle of 35° in relation to the "*e*" axis of the doubler crystal.[23] While the problem of controlling the polarization angle is easily solved by the introduction of a polarizer just in front of the conversion crystals, errors in tuning the crystals can be corrected by only a small amount. Typically, manual settings can routinely yield variations of about 100 μrad among our 24 beams. However, as discussed below, this amount of detuning does not contribute considerably to the overall nonuniformity present in our implosions.

The real impact of the conversion crystals on power imbalance comes when one considers the effects of their nonlinear response to input pulses with varying intensities. It can be seen in Fig. 41.8 that very significant perturbations in beam power can result due to the variance in conversion efficiency at the different input intensities. Any intensity variations among pulse shapes, such as those discussed in the previous section, can be significantly enhanced by the conversion process.

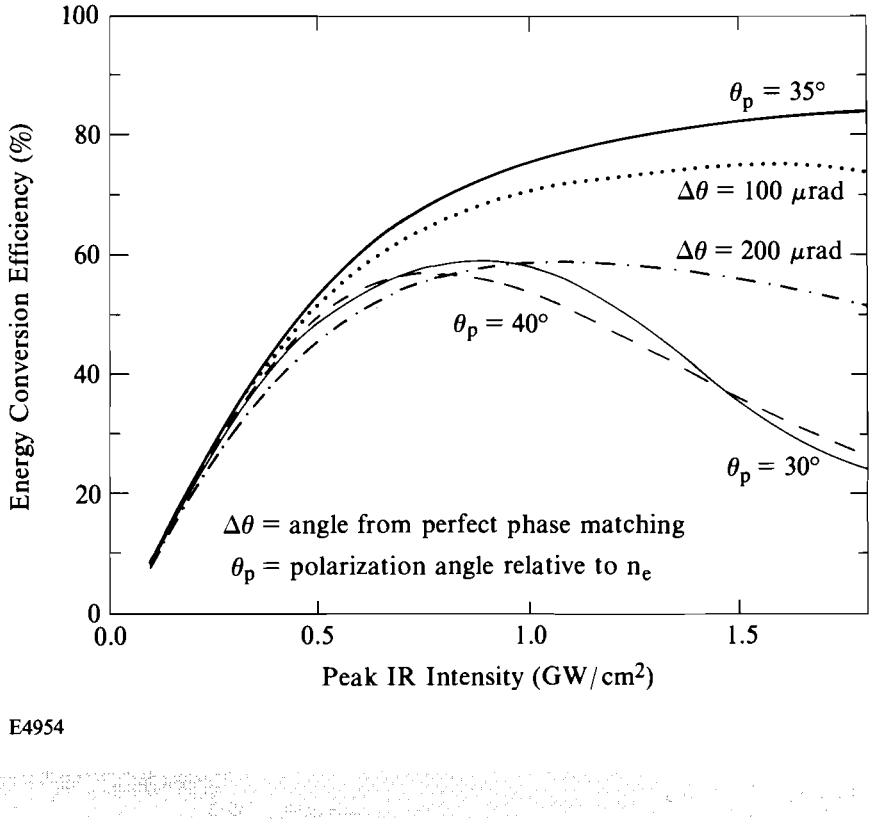

Fig. 41.8
Third-harmonic energy-conversion efficiency for type II - type II tripling in two 16-mm-thick KDP crystals for various tuning conditions.

To model the response of the conversion crystals, polynomial fits of the conversion efficiency as a function of the input intensity were obtained.[24] Such fits were provided for cases of optimal and 100-μrad detuning. At the beginning of each simulation, the crystal in each beamline was given a random detuning between optimal and 100 μrad that was fixed throughout the implosion. At each time step during the simulation, the input intensity into each crystal was calculated and an interpolation between the two fits provided the appropriately degraded conversion efficiency. These numbers were then factored into calculating the overall beam-balance factor used in distributing the energy over the sphere.

Transport Losses

The last effect to be modeled is transmission losses due to the system of transport optics that delivers the UV-converted light from the conversion crystals to the target. This system consists of turning mirrors, distributed phase plates (DPP's), focusing lenses, and blast windows. Any defects in these elements can affect the overall transport efficiency to the target. While the transmission characteristics of these elements can be tested to very high accuracy when removed from the OMEGA system, it has been very difficult to measure them while deployed on the system. Recently, however, a new system has been activated that can measure the transmission characteristics to within ±0.3%.[25] The OMEGA transport-integrating sphere (OTIS) can now routinely measure the transport on a weekly basis and has shown that variations in the transport efficiencies are in the range of ~5% peak-to-valley.

Using the information from the OTIS measurements, a simple fraction can be factored into the beam-balance factor. This number represents a static power imbalance throughout the pulse. As will be shown in the next section, variations in the transport losses in the range of 5% do not contribute significantly to the overall nonuniformities placed on target.

Numerical Evaluation of Power Imbalance

Using the numerical models described above, it is now possible to evaluate the effects of the various contributions on the level of nonuniformity. To provide a good approximation to our current experiments, the input power of each of the individual pulses is tuned to reflect the experimentally recorded, time-integrated energy balance. (Typically, the overall energy balance is in the range of 10% peak-to-valley.) We have chosen to use a laser-beam profile, shown in Fig. 41.9, that produces a level of nonuniformity characteristic of beams smoothed by spectral dispersion (SSD). This laser profile was constructed using a modified Airy pattern[9] of the form

$$I(\bar{r}) = g(\bar{r})\left[\frac{2J_1(\pi\bar{r})}{\pi\bar{r}}\right]^2,$$

where

$$\bar{r} = \left(r / r_o\right)_{\text{beam}} .$$

The function $g(\bar{r})$ includes the effects of small scale variations of the radial beam shape due to diffraction rings,[3] and is defined as

$$g(\bar{r}) = [1 + \epsilon \cos(\pi N \bar{r})].$$

Modulation parameters of $N = 3$ and $\epsilon = 0.1$ are used here.

We considered a typical OMEGA glass-ablator target that is shown schematically in Fig. 41.10. The pellet consists of a 5-μm-thick glass shell with an inner diameter of 240 μm and filled with 25 atm of deuterium. The target has been overcoated with 500 Å of aluminum to prevent any early shine-through effects.[26] *LILAC* was used to provide the time-dependent temperature and density profiles for this particular target when imploded by a 1300-J, 351-nm, 620-ps (FWHM) pulse. The nonuniformities due to four different scenarios were then calculated and the results appear in Fig. 41.11.

The first scenario simulated was the case of perfect power balance throughout the system. This result is shown as curve A in Fig. 41.11. One can see that initially the total nonuniformity is ~4% σ_{rms} and is in good agreement with other calculations done for the asymptotically smoothed SSD beam. To determine the source of this nonuniformity, it is possible to view the contributions for the individual ℓ-modes. Figures 41.12 and 41.13 show the distribution of the various ℓ-modes for each of the four scenarios at two times during the implosion (marked 1 and 2 in Fig. 41.11). Evaluating the particular modes for curve A, it can be seen that the nonuniformity is due solely to those modes that are affected by the beam-placement geometry of 24 beams (i.e., $\ell = 4$, 8, and 10).[3]

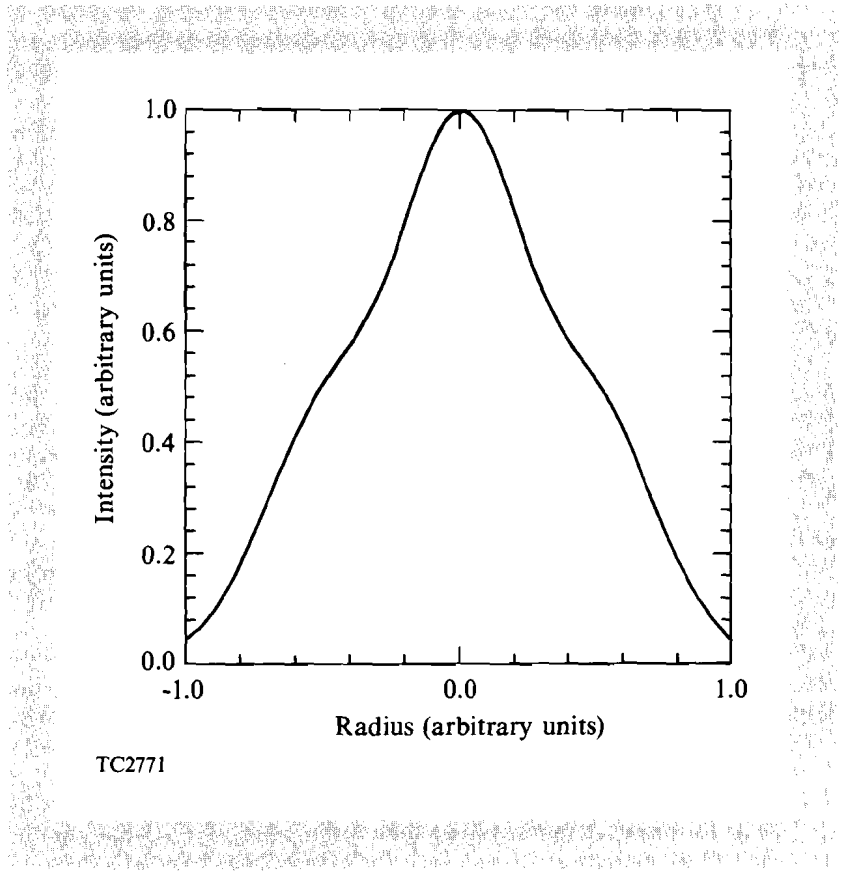

Fig. 41.9
Asymptotically smoothed, SSD laser-beam profile used in the calculations.

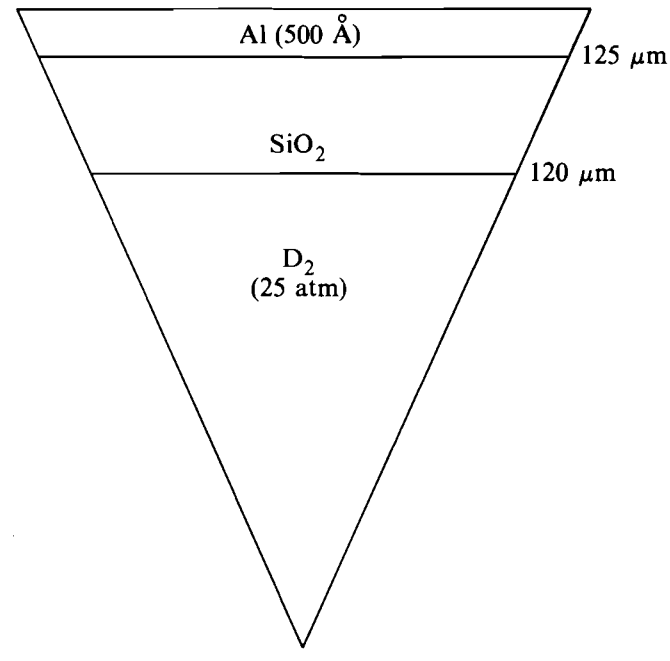

Fig. 41.10
Schematic of a single-shell, glass-ablator, OMEGA high-density pellet.

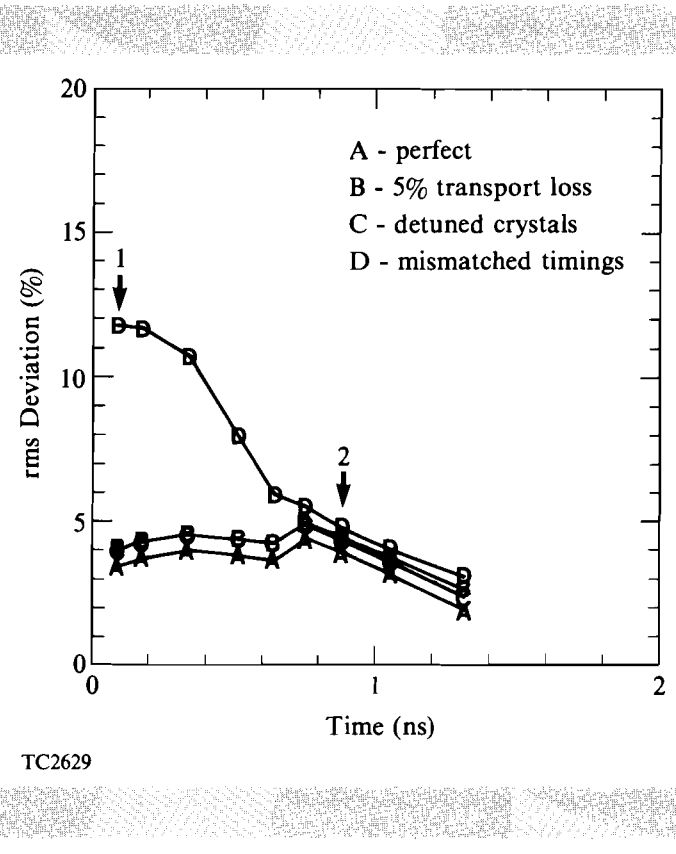

Fig. 41.11
Calculated rms deviation for four different illumination scenarios.
(A) Perfect power balance throughout the laser system.
(B) 5% peak-to-valley random variations in the transport optics in each of the 24 OMEGA beamlines.
(C) In addition to B, a random detuning in each of the 24 frequency-conversion crystals from 0 to 100 μrad.
(D) Including B and C, a 5% random variation in both beam-arrival time and FWHM.

The ℓ-mode spectra at times 1 (30 ps) and 2 (900 ps) in the implosion are given in Figs. 41.12 and 41.13, respectively.

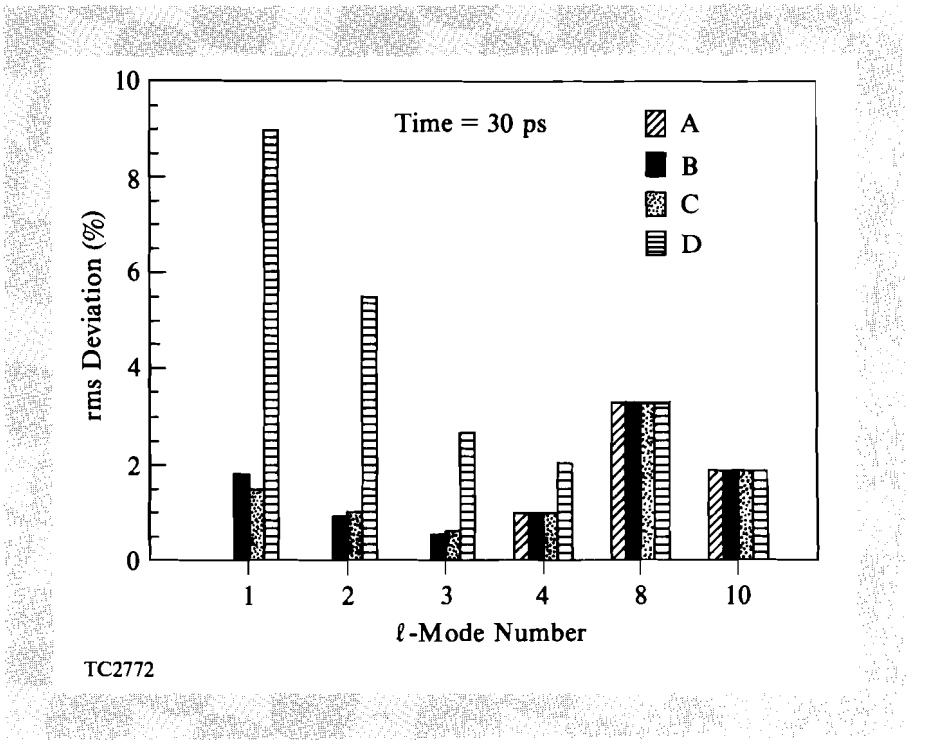

Fig. 41.12
Legendre ℓ-mode spectrum evaluated at 30 ps into the implosion. (This corresponds to point 1 in Fig. 41.11).

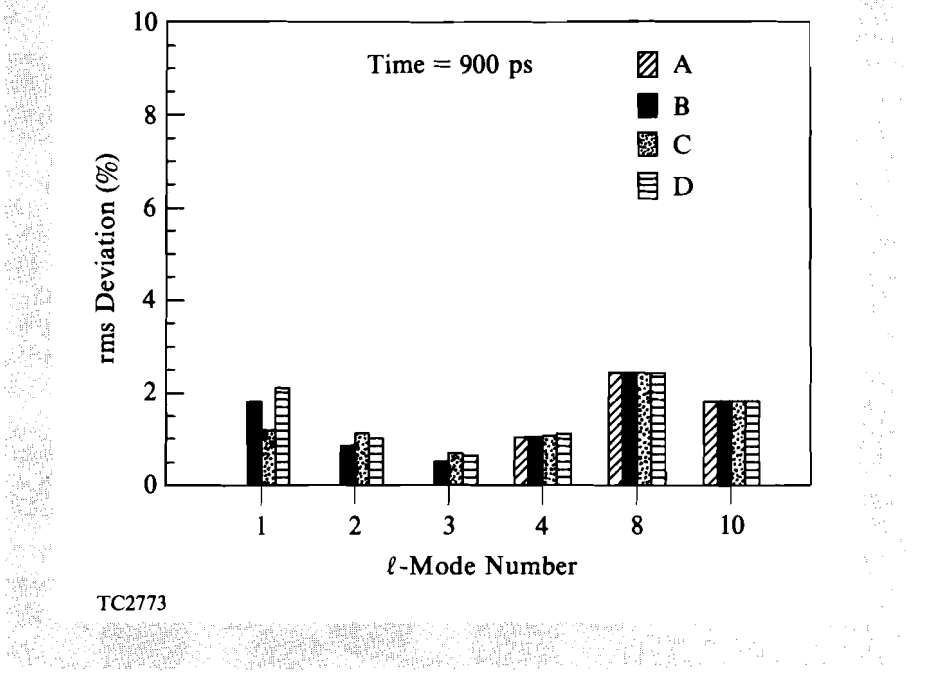

Fig. 41.13
Legendre ℓ-mode spectrum evaluated at 900 ps into the implosion. (This corresponds to point 2 in Fig. 41.11).

The second scenario assumed that the transport losses between the frequency-conversion crystals and the target have a random 5% peak-to-valley variation among all beams. From curve B in Fig. 41.11 we see a modest increase in the applied nonuniformity as a function of time. Examining the ℓ-mode distribution, it can be seen that there are now contributions from the $\ell = 1, 2$, and 3 modes. These contributions are almost constant throughout the implosion, as can be seen from Fig. 41.13.

The next scenario considered the application of a random detuning from 0 to 100 μrad to each of the 24 conversion crystals in addition to the 5% transport variations of the second scenario. The results of this third scenario are shown as curve C in Fig. 41.11. The fact that there is very little difference between the second and third scenarios illustrates how the various contributions to nonuniformity add in quadrature, so that even though the applied spectrum can differ, the overall effect can remain unchanged or, in some cases, actually improve.

In the last scenario we attempt to fully model all of the factors contributing to power imbalance on OMEGA. In addition to the factors of the third scenario, the arrival times and shapes of all 24 laser pulses are each randomly varied by 5% peak-to-valley. Such pulse variations lead to a much higher total nonuniformity level early in the implosion as can be seen from curve D in Fig. 41.11. All modes from $\ell = 1$ to 4 are significantly excited early in the implosion. However, as the implosion proceeds, the power balance among the individual beams improves and we recover the results of the second and third scenarios. This can also be seen in Fig. 41.13 where the highly excited low-order modes seen in Fig. 41.12 have calmed down significantly.

Reviewing the results of the four separate scenarios, it can be seen that our efforts to characterize and correct problems with transport losses and conversion-crystal detuning have resulted in these factors making only a small contribution to the overall level of nonuniformity on target. However, as the fourth scenario illustrates, problems with pulse shapes and timing can lead to very large pertubations at early times in our implosions.

Power-Imbalance Experiment

Experimental verification of the calculated nonuniformity levels within ICF targets is a major goal of the LLE direct-drive program. However, there have been few, if any, experimental diagnostics available with the spatial and temporal resolution required to provide useful information about the existence of the predicted nonuniformities. Recently, however, with the advent of the x-ray-framing cameras developed at the Lawrence Livermore National Laboratory (LLNL),[27] it has become possible to diagnose relatively long duration ($\gtrsim$ 50-ps), large (>10-μm) perturbations during the implosion. The serpentine x-ray-framing camera,[28, 29] shown schematically in Fig. 41.14, allows for 14 x-ray images, separated by ~47 ps, during the implosion. The spatial resolution is determined by the individual size of each pinhole in the pinhole array. (For our camera this is typically 12 μm.) The deployment of this diagnostic on OMEGA has enabled the characterization of an experiment in which a deliberate power imbalance was applied. The level of nonuniformity present in the experiment was calculated and then used in a two-dimensional *ORCHID* simulation. The correlation of experiment and simulation tends to validate our estimates of the nonuniformity present.

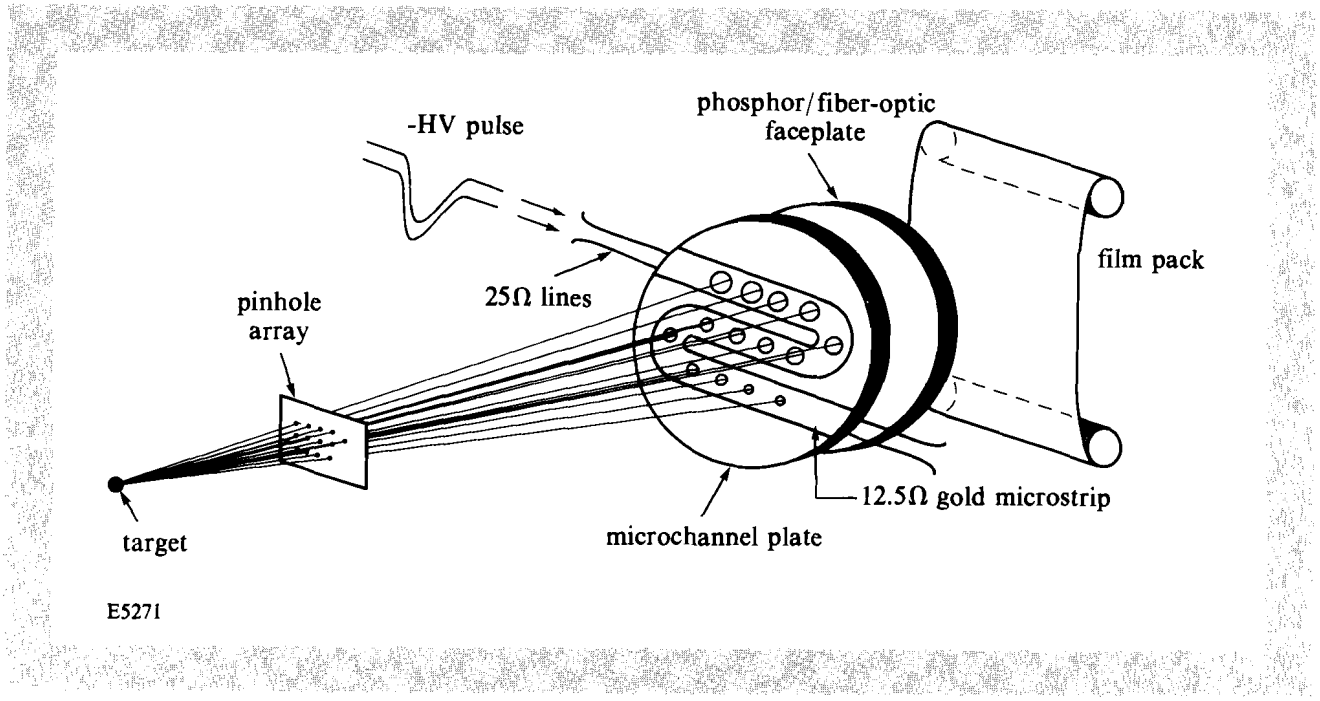

Fig. 41.14
Schematic of the serpentine x-ray-framing camera deployed on the OMEGA laser system.

The design of a power-imbalance experiment presented two challenges. The first involved manipulating the laser beams such that a particular mode would be imprinted on the target with sufficient strength to both dominate all other modes present and be detectable by the diagnostic. The second challenge was based on our desire to use *ORCHID* to simulate the implosion. Because *ORCHID* assumes azimuthal symmetry, it was necessary to isolate the pure $m = 0$ component of the imprinted ℓ-mode.

The mode we chose to imprint was the $\ell = 1$ mode. This was accomplished by employing beam clusters 2 and 5 on the OMEGA laser system. The energy of these beams was increased (cluster 2) or decreased (cluster 5) by ~20% from the mean. It was estimated that a ~ 40% peak-to-valley, $\ell = 1$ mode should then result on target. The decomposition of this illumination pattern, given in Fig. 41.15, confirmed the large $\ell = 1$ contribution imprinted on target. Analysis of the phase information identified several ports on the OMEGA target chamber, including port #133, whose lines of sight were almost directly perpendicular to the plane formed between clusters 2 and 5. Using the orientation of port #133, 96% of the $\ell = 1$ mode exists in the $m = 0$ harmonic (i.e., almost purely azimuthally symmetric). The serpentine camera was positioned in port #133 such that the applied illumination pattern would be recorded with the maximum intensity of cluster 2 on the left-hand edge of the film plane.

The data from this experiment are shown in Fig. 41.16. As the implosion proceeds (the frames follow a reversed "*S*" configuration with time), it can be seen that the imploded core is in fact pushed off center by the applied

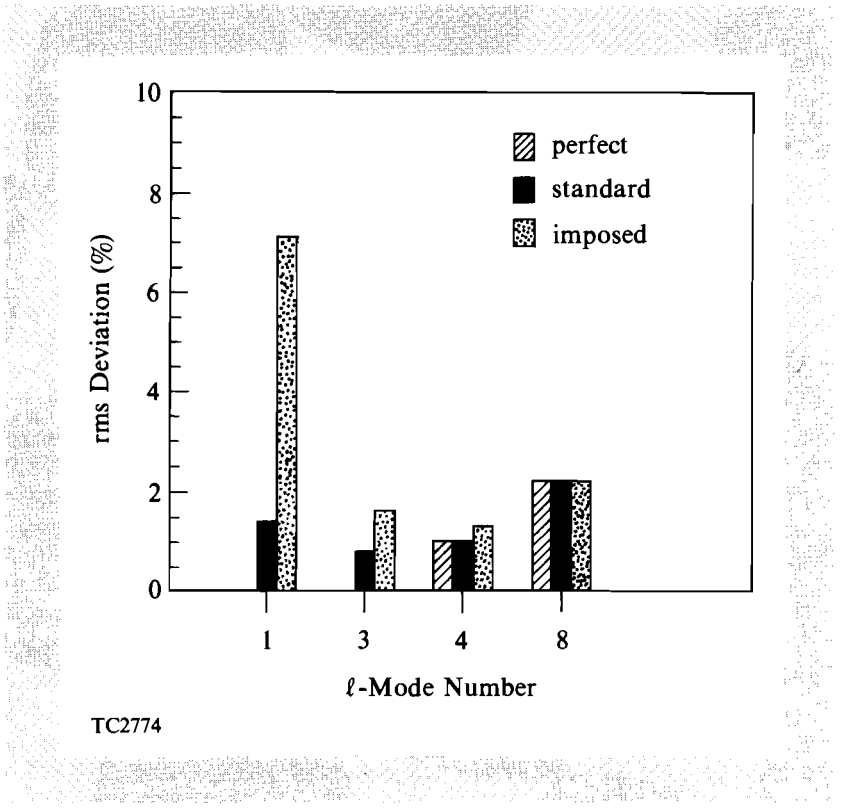

Fig. 41.15
Comparison of the calculated ℓ-mode spectra for perfect power balance, typical OMEGA power imbalance, and the imposed power-imbalance experiment.

perturbation. In Fig. 41.17 we have selected an individual frame for analysis that is approximately 300 ps after the peak of the pulse. The geometric center of the limb emission for this frame was determined and an azimuthal average gives the intensity as a function of the radial position as shown in Fig. 41.18. From Fig. 41.18, it can be seen that the core has formed approximately 6 μm to 10 μm to the right of center during the implosion. The limbs appear almost circular and are located at ~ ±45 μm from the center.

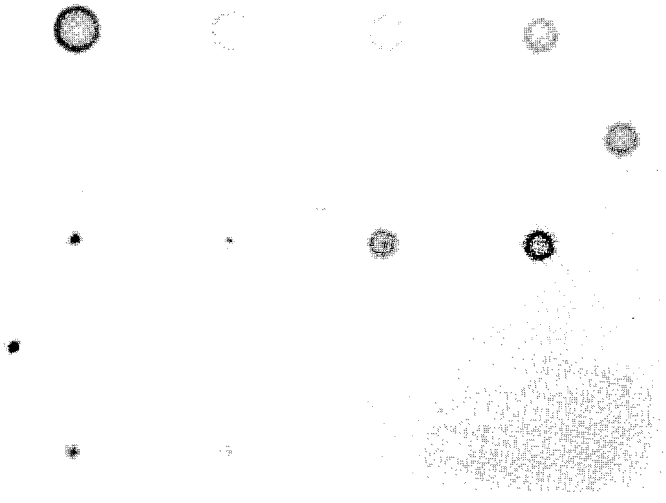

Fig. 41.16
Experimental data obtained using the serpentine x-ray-framing camera for OMEGA shot #18682. The initial target diameter was 250 μm. The individual frames are separated by ~47 ps and are "open" for ~100 ps.

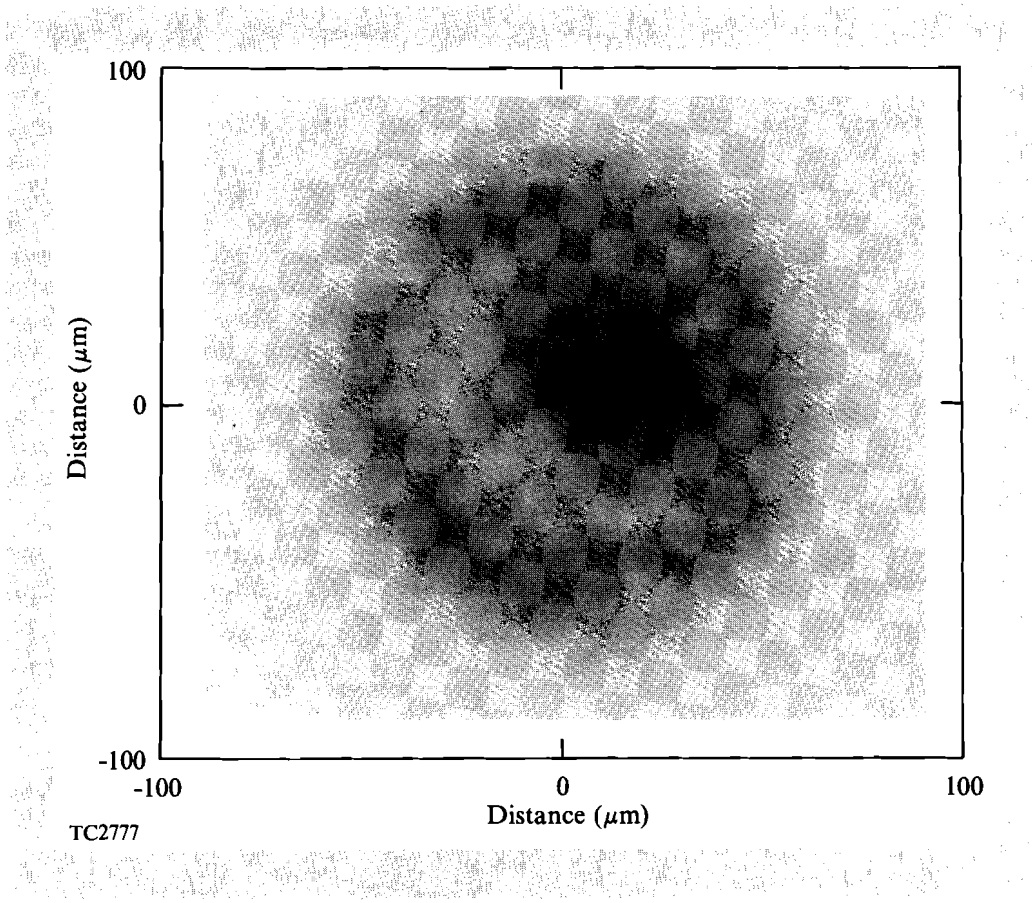

Fig. 41.17
Individual x-ray-framing image taken from Fig. 41.16 (frame H). This particular frame was approximately 300 ps after the peak of the pulse.

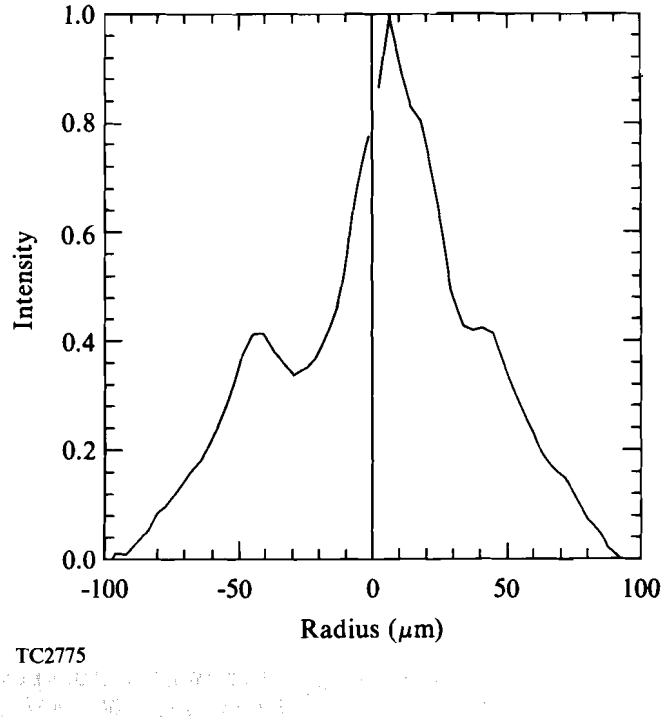

Fig. 41.18
Azimuthally averaged intensity profiles over both left- and right-hand sides of image shown in Fig. 41.17. An average about the geometric center of the limb emission is used to obtain each profile.

The time-dependent nonuniformity calculated for this implosion was then used as input to an *ORCHID* simulation. Only the dominant modes ($\ell = 1, 2, 3$, and 8) were simulated. The implosion was simulated to a time that was comparable to the frame chosen and the results are presented in Fig. 41.19. From the grid plot [Fig. 41.19(a)], the simulation prediction for the position of the imploded core is close to that observed in the experiment. Determination of the limb-emission location requires evaluating a contour plot of the electron temperature. The limb emission should peak in the region between 800 eV to 1000 eV. The electron-temperature isotherms are plotted in Fig. 41.19(b) and the position of the 800-eV isotherm, relative to the center of the implosion, is again in good agreement with the experimental data. This correlation between the experiment and simulation is very encouraging. We hope to repeat a more extensive set of these experiments, evaluating not only other ℓ-modes, but also examining how the overall target performance (i.e., neutron yield) is affected by the presence of various applied nonuniformities.

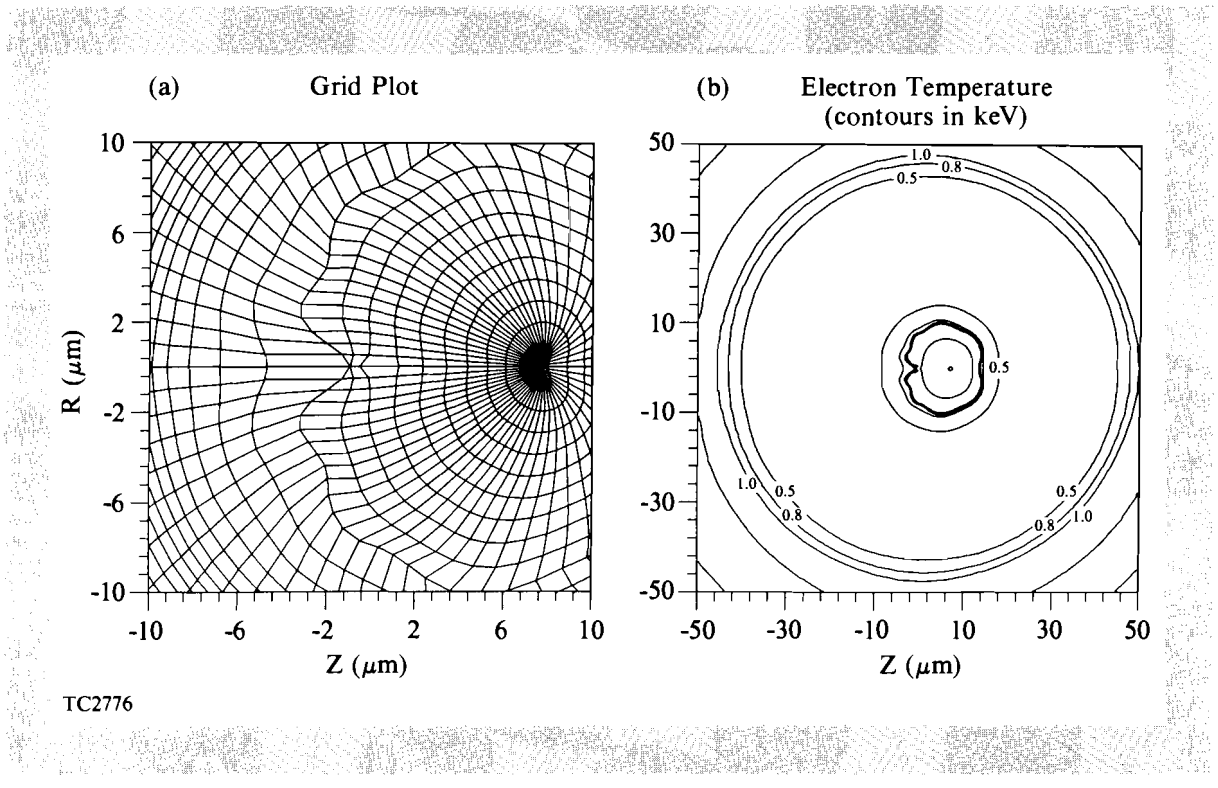

Fig. 41.19
Two-dimensional (*ORCHID*) hydrodynamics simulation of the single-shell OMEGA target shown in Fig. 41.11.

(a) The grid plot has been expanded to display the position of the imploded core at 1290 ps into the implosion. The core has formed ~7 μm to the right of center.

(b) Contour map of the electron temperature at 1290 ps into the implosion. The limb emission (~800 eV to 1000 eV) is predicted to be circular with a radius of ~45 μm.

Conclusion

Power imbalance among the 24 OMEGA laser beams can produce significant long-wavelength irradiation nonuniformities on target during implosions. We have adapted our uniformity codes to incorporate time-

dependent density and temperature profiles obtained from *LILAC* simulations of the experiments. The various sources of power imbalance on the OMEGA system have been characterized and modeled numerically. From the analysis it has been shown that the levels of power imbalance due to frequency-conversion crystal detuning and UV-transport losses, when managed properly, make only a modest contribution to the overall nonuniformity. However, this analysis also shows that significant nonuniformity can be imprinted on the target early in the implosion due to pulse misshaping. Finally, an experiment involving deliberately applied levels of power imbalance was undertaken and then simulated with *ORCHID* using estimates of the applied perturbation. Good correlation was found between the experimentally observed core positions and those predicted by the *ORCHID* simulation. Further experimental investigations are in progress.

ACKNOWLEDGMENT

This work was supported by the U.S. Department of Energy Division of Inertial Fusion under agreement No. DE-FC03-85DP40200 and by the Laser Fusion Feasibility Project at the Laboratory for Laser Energetics, which has the following sponsors: Empire State Electric Energy Research Corporation, New York State Energy Research and Development Authority, Ontario Hydro, and the University of Rochester.

REFERENCES

1. S. E. Bodner, *J. Fusion Energy* **1**, 221 (1981).
2. J. H. Nuckolls, *Phys. Today* **35**, 24 (1982).
3. S. Skupsky and K. Lee, *J. Appl. Phys.* **54**, 3662 (1983).
4. S. Skupsky, R. L. McCrory, R. S. Craxton, J. Delettrez, R. Epstein, K. Lee, and C. P. Verdon, *Laser Interaction and Related Plasma Phenomena*, edited by H. Hora and G. H. Miley (Plenum, New York, 1984), Vol. 6, p. 751.
5. LLE Review **23**, 125 (1985).
6. LLE Review **37**, 1 (1988).
7. J. Nuckolls, L. Wood, A. Thiessen, and G. Zimmerman, *Nature* **239**, 139 (1972).
8. LLE Review **37**, 1 (1988).
9. LLE Review **33**, 1 (1987).
10. LLE Review **37**, 29 (1888).
11. LLE Review **37**, 40 (1988).
12. S. Skupsky and T. Kessler, *Opt. Commun.* **70**, 123 (1989).
13. S. Skupsky, R. W. Short, T. Kessler, R. S. Craxton, S. Letzring, and J. M. Soures, *J. Appl. Phys.* **66**, 3456 (1989).
14. *Laser Program Annual Report, 1974*, #UCRL-50021-74, edited by J. I. Davis and W. Clements [(California University, Lawrence Livermore Laboratory, Livermore (USA), 1975)], p. 519.
15. J. E. Howard, *Appl. Opt.* **16**, 2764 (1977).
16. A. J. Scannapieco and H. Brysk, *J. Appl. Phys.* **50**, 5142 (1979).
17. LLE Lab Report No. 88 (1981).

18. LLE Lab Report No. 16 (1973).

19. A. J. Schmitt and J. H. Gardner, *J. Appl. Phys.* **60**, 6 (1986).

20. G. B. Arfken, *Mathematical Methods for Physicists*, 3rd ed. (Academic Press, New York, 1985), p. 683.

21. P. A. Jaanimagi, J. Kelly, R. Keck, W. Seka, and R. Saunders, *Bull. Am. Phys. Soc.* **34**, 2041 (1989).

22. R. L. Keck, J. P. Knauer, S. Letzring, S. Morse, W. D. Seka, and J. M. Soures, *Bull. Am. Phys. Soc.* **34**, 2041 (1989).

23. R. S. Craxton, *Opt. Commun.* **34**, 474 (1980).

24. R. S. Craxton and J. P. Knauer (private communication).

25. LLE Review **38**, 111 (1989).

26. LLE Review **35**, 125 (1988).

27. J. D. Kilkenny *et al.*, *Rev. Sci. Instrum.* **59**, 1793 (1988).

28. D. K. Bradley, J. Delettrez, P. A. Jaanimagi, C. P. Verdon, J. D. Kilkenny, and P. Bell, *Bull. Am. Phys. Soc.* **34**, 1962 (1989).

29. P. E. Bell, J. D. Kilkenny, G. Power, R. Bonner, and D. K. Bradley, *Ultra High Speed Photography, Videography, and Photonics VII* (SPIE, Bellingham, WA, 1989), to be published.

Section 2
ADVANCED TECHNOLOGY DEVELOPMENTS

2.A Laser-Beam Apodizer Utilizing Gradient-Index Optical Effects in Liquid Crystals

Laser-beam apodization has been a goal of solid-state laser programs since the early 1970s. Apodization is the shaping of the spatial beam profile to increase the fill factor through the gain medium. This allows more energy to be extracted and also reduces linear and nonlinear edge-diffraction effects that cause self-focusing spikes. A beam apodizer determines, to a large extent, the ultimate performance of a high-power laser system.

An ideal beam apodizer possesses the following characteristics[1]:

1. The slope of the transmission function should be such that the radial distance between the 90% and 10% transmission points is at least $3\lambda L/d$, where λ is the laser wavelength, L is the propagation distance over which intensity modulation should be minimal, and d is the beam diameter. One of the transmission functions that approximates this condition is a super-Gaussian of order N, that is,

$$T(r) = \exp\left[-(r/r_o)^N\right], \tag{1}$$

where the radial clear aperture r_o is selected based on the condition that $T(r_1) = 10^{-3}$, where $2r_1$ is the entry aperture of the amplifying device that follows the apodizer.

2. Wave-front quality over the clear aperture and into the soft edge is a smooth function with continuous first derivatives.

3. The peak-to-minimum transmission ratio is at least 1000 to 1.
4. High laser-damage threshold at the design wavelength and pulse width.
5. Environmental stability.

Several techniques for apodizing laser beams have been reported.[1–11] Recently, S. D. Jacobs *et al.* have developed a new apodizer based on liquid-crystal technology that has demonstrated properties resembling those of a perfect apodizer.[12] However, their device concept works best for small clear apertures, and the exponential relationship used to model the reflectivity of their cholesteric liquid crystal (CLC) as a function of thickness is valid only as a first approximation.

In this article, we propose a novel beam apodizer utilizing the fluid-like properties of CLC's for beam apodization of slab-geometry amplifiers or diode lasers, and also for beam apodization of rod amplifiers with large clear apertures. We will briefly review the optical properties of CLC's and then explore the design concepts of two beam apodizers based on a gradient-index optical effect in these fluids.

Optical Properties of Cholesteric Liquid Crystals

CLC's have a helical layered organization as shown in Fig. 41.20. Normally, a CLC cell is prepared between two glass substrates. Within each single layer of the structure, molecules align in a parallel configuration like nematics. The average orientation of the elongated liquid-crystal molecules is defined as the director. In adjacent layers, protruding side groups of atoms attached to each molecule force the director to be twisted. The rotation of layers through the fluid gives rise to a helical structure. One full 360° rotation of the director is defined as one pitch length P_o. This helical structure leads to the important optical property of selective reflection in circular polarization and wavelength.[13]

Our CLC's are a blend of a nematic liquid crystal and a chiral additive. The selective-reflection peak wavelength can be tuned by changing the blending ratio (or relative concentration) of these materials. In blending, adding more nematic liquid crystal increases the pitch length P_o and adding more chiral additive decreases P_o.

In Fig. 41.20 we consider a right-handed CLC cell whose helical axis is oriented along the z-axis. No interaction occurs between the right-handed helical structure of the CLC and left-handed circularly polarized light propagating through it. However, when right-handed circularly polarized light with wavelength λ propagates along the z-axis at normal incidence, the reflectivity R is given by[14]

$$R = \frac{\sin^2\left[\kappa L\sqrt{1-(\delta/\kappa)^2}\right]}{\cosh^2\left[\kappa L\sqrt{1-(\delta/\kappa)^2}\right]-(\delta/\kappa)^2}, \tag{2}$$

where $\kappa = \kappa_o \cdot (\lambda_o/\lambda)$ and $\kappa_o = (\pi/\lambda_o) \cdot \Delta n$ is the coupling coefficient; $\delta = 2\pi\,(1/\lambda - 1/\lambda_o)n_{av}$ is the detuning parameter; $\lambda_o = n_{av} \cdot P_o$ is the peak wavelength of the selective reflection band; and L is the CLC fluid thickness.

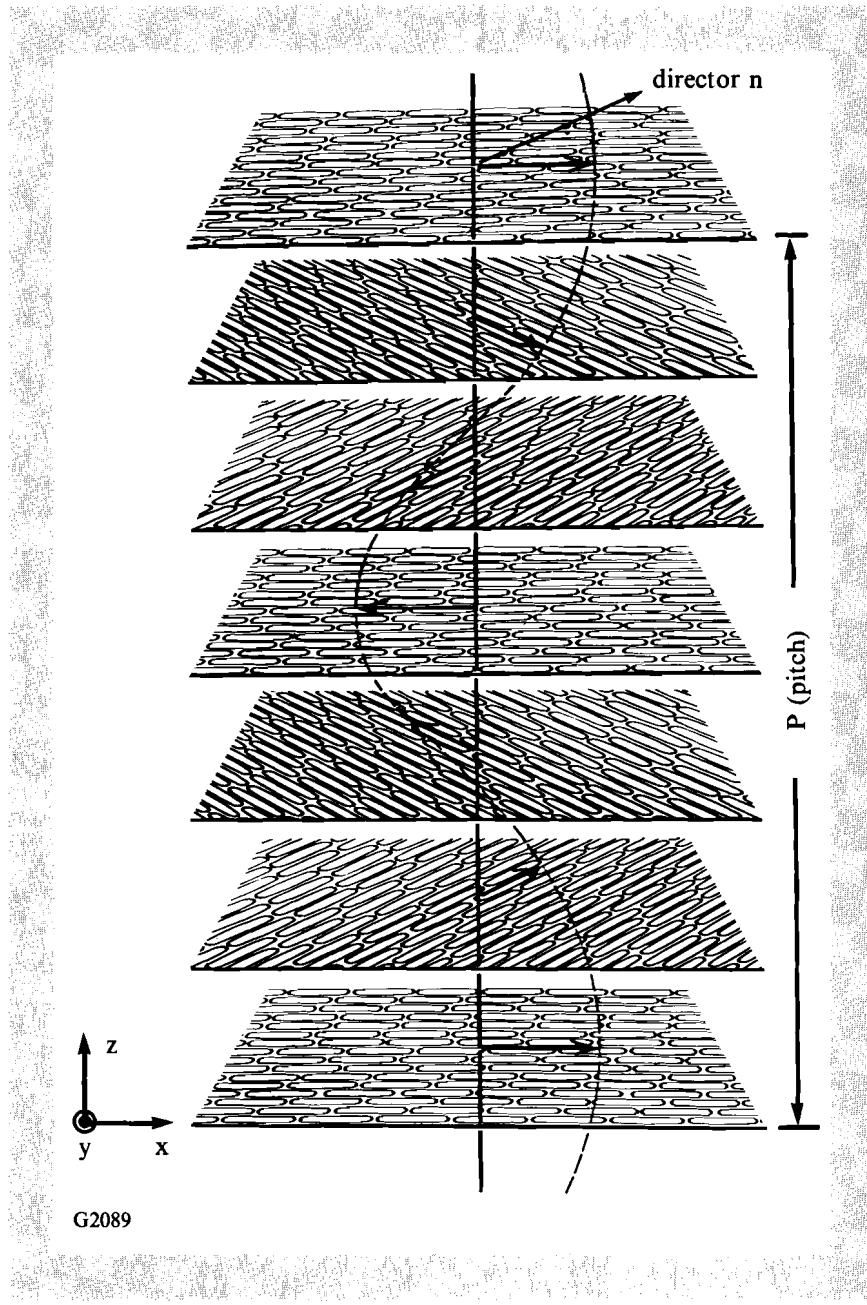

Fig. 41.20
Schematic diagram of molecular order in a cholesteric liquid crystal.

Here, Δn and n_{av} represent the optical birefringence and average refractive index, respectively. When $\lambda = \lambda_o$, the CLC structure is well phase matched to the input wavelength, and the reflectivity is equal to

$$R = \tanh^2(\kappa_o L). \quad (3)$$

A wedged cell was fabricated to confirm the relationship in Eq. (3) using the blend of a nematic liquid crystal E7 and chiral additive CB15 tuned to

exhibit a selective reflection peak at λ = 1064 nm. (The liquid-crystal compounds for this work were purchased from EM Chemicals, Hawthorne, NY, and used as received.) For the CLC fluid prepared, $n_{o,n} = 1.4172, n_{e,n} = 1.6014, \Delta n = 0.1842$, and $n_{av} = 1.5093$ as determined with an Abbé refractometer (22°C, λ = 1053 nm). At λ = 1064 nm, the coupling coefficient is calculated to be $\kappa_o \cong 0.5480$. For this CLC blend, the reflectivity as a function of thickness is shown in Fig. 41.21. The close match of theoretical and experimental data supports the validity of Eq. (3).

A plot of the reflectivity R as a function of λ/λ_o for $\kappa L = 4.59$ is shown in Fig. 41.22. It can be seen that when $\lambda/\lambda_o = 1.076$, the reflectivity of the CLC goes to zero. The ripples in Fig. 41.22 are due to phase mismatching. This effect is not seen in practice for cells assembled with weak surface

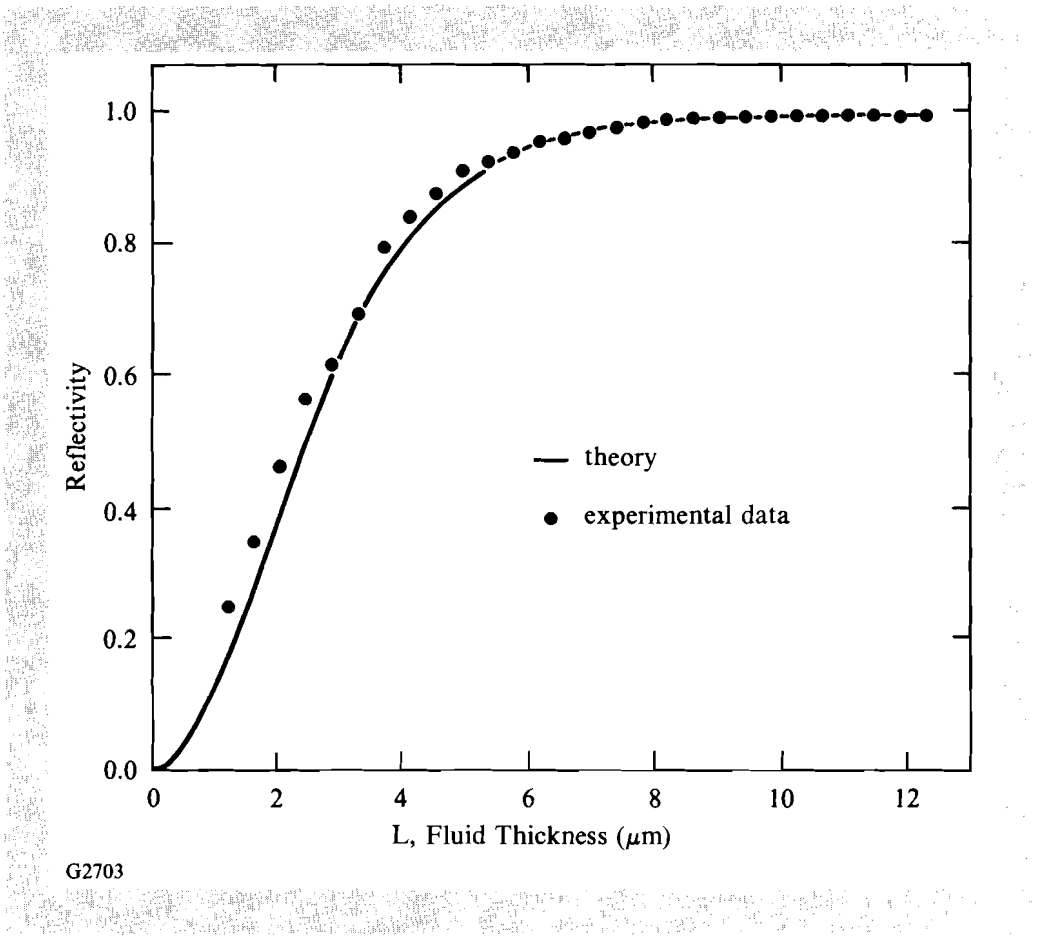

Fig. 41.21
Reflectivity R measured at λ = 1064 nm, as a function of thickness L, for a mixture of E7 and CB15 tuned to exhibit a selective peak at λ_o = 1064 nm. The coupling coefficient κ_o is 0.5439. The solid line represents the result of theoretical calculation, and the circles represent experimental data.

anchoring due to the presence of small nonuniformities through the bulk of the fluid. This weak surface anchoring (at one or both of the inner surfaces of the cell) is very important for the apodizer application described here because it prevents any discontinuity in structure[15] and concomitant deviations from a smooth reflectivity profile.

A spatial gradient in selective-reflection peak wavelength can be induced by filling a device with mixtures of two CLC fluids having different selective-reflection bands, from opposite sides of a cell as shown in Fig.

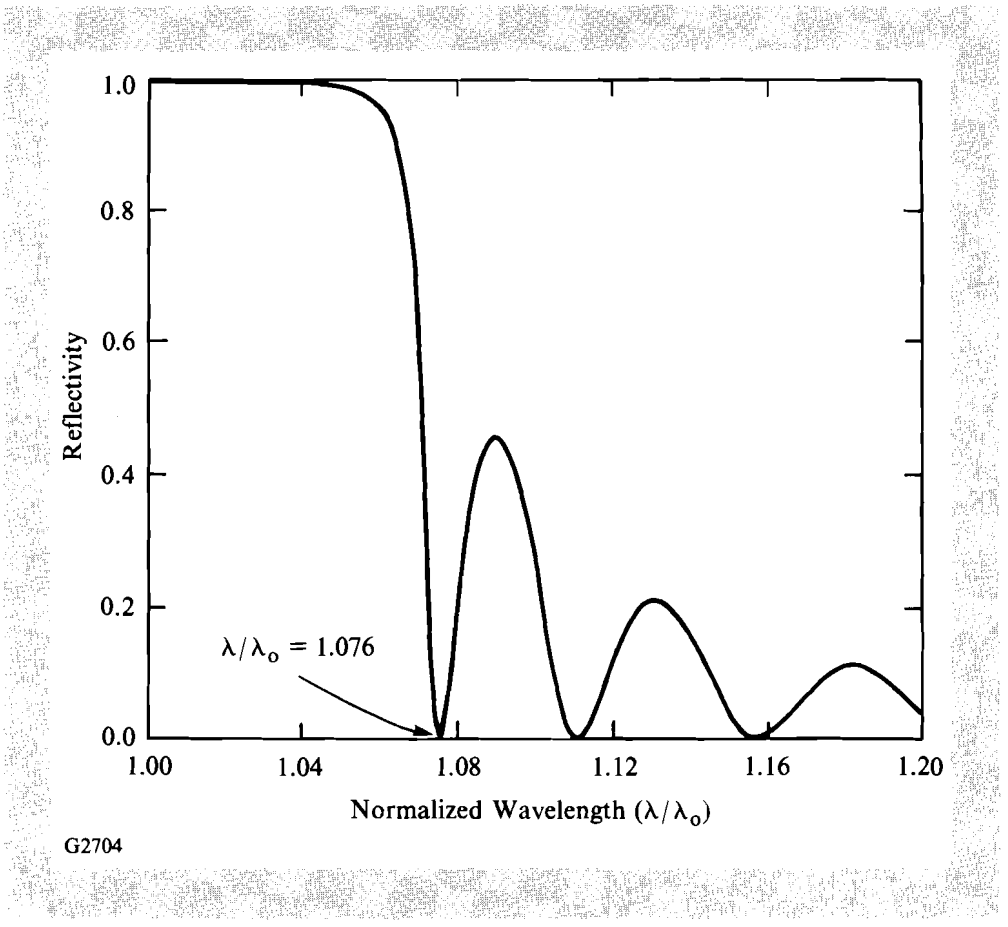

Fig. 41.22
Reflectivity R as a function of normalized wavelength λ/λ_o for $\kappa L = 4.59$.

41.23. The fluid-like property of liquid crystals allows them to blend together in region 3. This concept will be referred to as a gradient CLC (GCLC). The blending ratio (relative concentration) of chiral additives in the nematic liquid-crystal host varies linearly in region 3 from the region-1 side to the region-2 side. Since the helix wave number of the CLC, $q_o = 2\pi/P_o$, is proportional to the concentration,[16] δ/κ in Eq. (2) can be rewritten as

$$\frac{\delta}{\kappa}(x) = \frac{2n_{av}}{\Delta n}\left[1-\frac{q_o(x)}{k_o}\right] = \frac{2n_{av}}{\Delta n}\left(1-\frac{\lambda_o}{\lambda}\right), \tag{4}$$

where $k_o = (2\pi/\lambda) \cdot n_{av}$ is the wave number in the liquid-crystal medium. For simplicity, the average refractive index and birefringence are assumed to be constant in the wavelength regions of interest. Then λ/λ_o changes linearly as a function of position. If two CLC's are chosen such that CLC2 has a normalized wavelength λ/λ_o that gives rise to high reflectivity and CLC1 has $\lambda/\lambda_o = 1.076$, a smooth-edge profile can be created in the overlap region as shown in Fig. 41.23. Assuming that the width of the overlap region is held constant, the slope of the transmission function across the overlap region can be varied by tuning the λ/λ_o of CLC2 used for high reflection in region 2 of Fig. 41.23. As the λ/λ_o in region 2 approaches 1.076, the slope across the

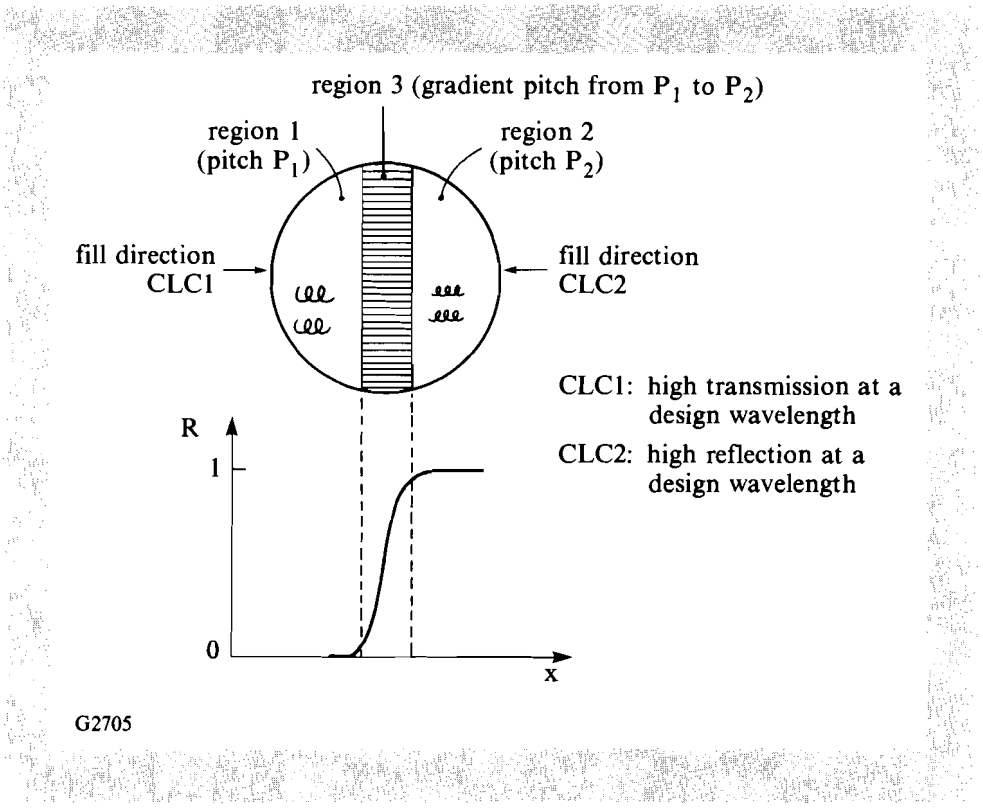

Fig. 41.23
Reflectivity profile for a gradient cholesteric liquid-crystal element. The fluid-like property of cholesteric liquid crystals allows them to mix over a finite region of contact and create a pitch gradient. This results in a smoothly varying reflectivity profile.

overlap region (region 3) is reduced, resulting in a softer reflectivity edge profile for the device.

There are several ways to create shaped gradients in Δn and n_{av}: (1) by using the same host nematic with different concentrations of the same chiral additive resulting in two distinctly different selective-reflection bands with similar Δn; (2) by using different host nematics (allowing for variability in viscosity and birefringence) with the same chiral additive; and (3) by using different host nematics with different chiral additives.

Implementation of Beam Apodizers

1. One-dimensional apodizer

Three cleaned, uncoated, nearly identical 38-mm-diameter GCLC cells were assembled from borosilicate glass (BK-7) substrates. For each cell, the gap thickness was set at 13 μm with Mylar® spacers. Filling was done by capillary action at 60°C, above the isotropic transition temperature of nematic E7, with two different right-handed CLC blends, each containing a different amount of the chiral additive CB15. One CLC was tuned to exhibit a selective-reflection peak at $\lambda_o = 1064$ nm at 22°C, the other at $\lambda_o = 820$ nm. A near-planar structure was produced by the usual method of shearing. Figure 41.24 gives reflection spectra in the form of optical density for each

CLC mixture in the visible and near infrared at 22°C. These spectral scans were taken with unpolarized optical radiation in a spectrophotometer (Perkin-Elmer Lambda-9). As mentioned earlier, the side lobes (or ripples) do not appear in spectra under conditions of weak anchoring, due to the nonuniformities in helix wave number of the molecules in the bulk. The slight tilt of the flat-top region and the asymmetric selective-reflection peak shapes in these scans come from a slight tilt in the planar structure induced by inner-substrate surface effects. The degree of selective reflection, as indicated by the magnitude of the change in optical density, ΔO.D., from the base line, is equal to about 0.29, which shows good alignment. (The theoretical limiting value is equal to log 2 = 0.3.)

The experimental setup used to measure apodizer transmission profiles is shown in Fig. 41.25(a). The output of a diode-pumped Nd:YAG laser (Amoco Micro Laser at 1064 nm) is converted to right-handed circularly polarized light, collimated and focused onto a GCLC cell (500-μm spot size).

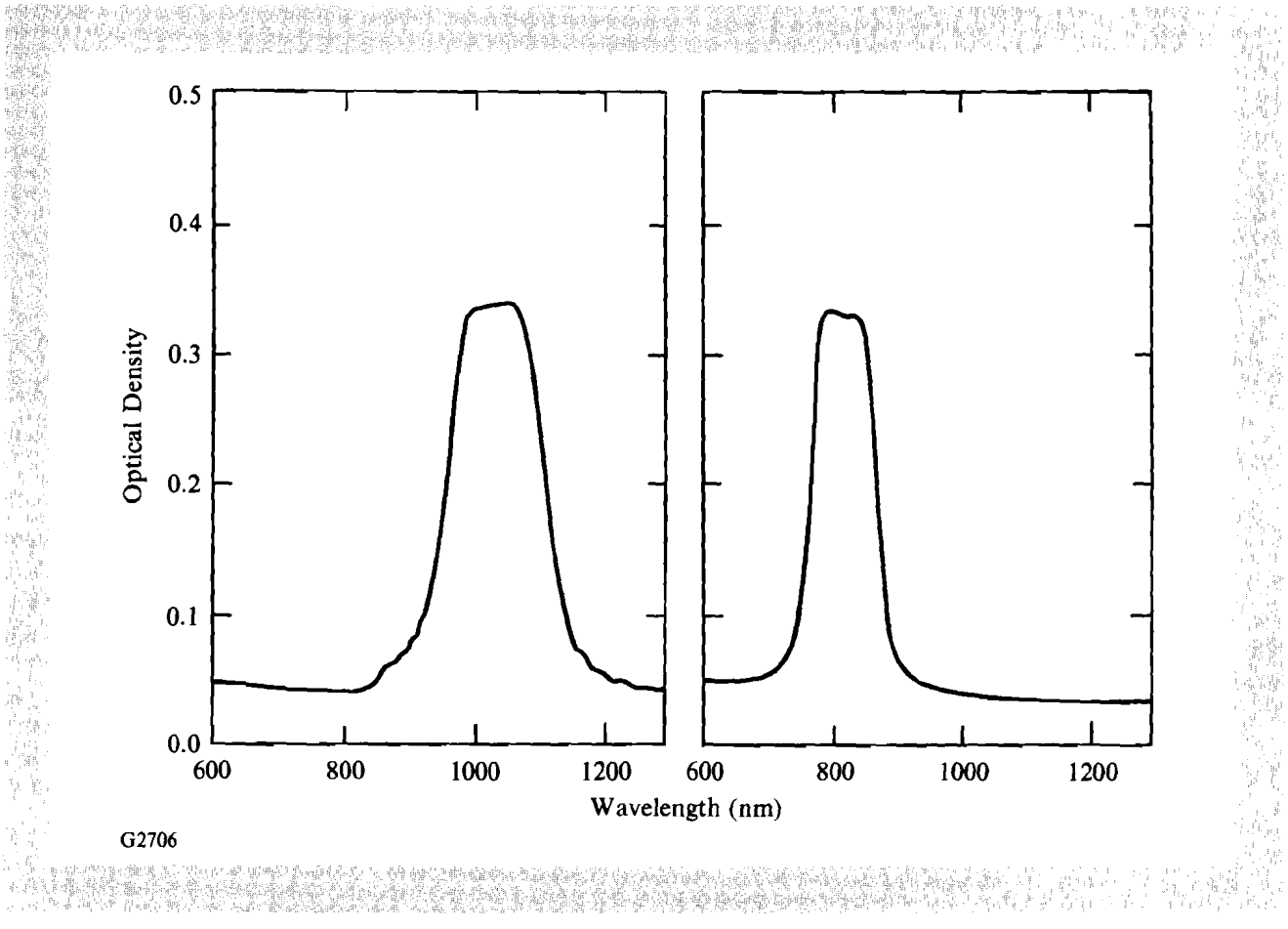

Fig. 41.24
Individual selective-reflection bands for two different cholesteric liquid crystals used in fabricating a GCLC element.

The cell is scanned by passing through the beam on a translation stage. Transmitted light intensity is measured using a photodiode detector (United Detector Technologies, UDT-10). Figure 41.25(b) shows the transmission profiles of the three GCLC cells taken at $T = 22$°C. The size of the interface region is determined and can be controlled by the length of time during which the filled device is annealed at a temperature above the isotropic phase-

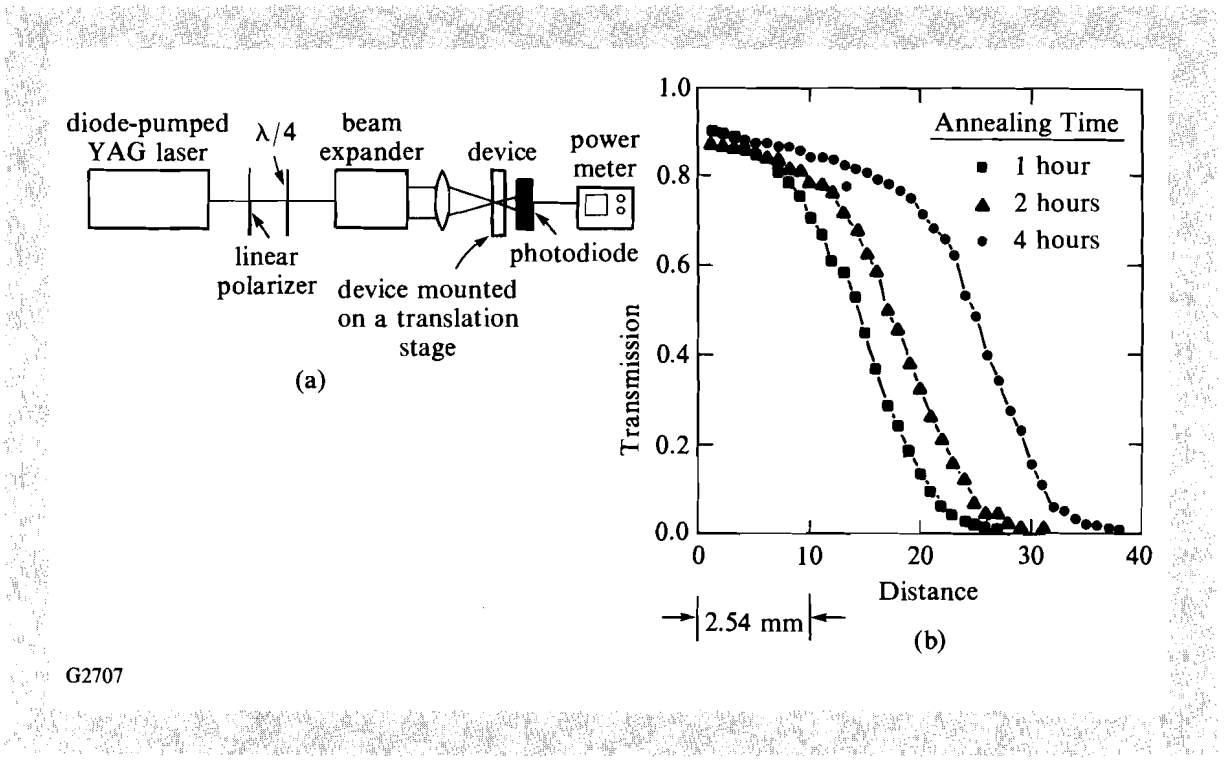

Fig. 41.25
(a) Experimental apparatus used to measure transmission profiles of apodizers.
(b) Transmission profiles for three gradient GCLC's as a function of position after annealing periods of 1 h, 2 h, and 4 h in the isotropic phase.

transition temperature of the mixtures. This keeps fluid viscosity low and permits *in situ* blending to occur.

The concept of controlled fluid blending to create a linear optical gradient can be exploited to make a one-dimensional rectangular beam apodizer as shown in Fig. 41.26. This device can be constructed by taking two nearly identical GCLC cells whose fabrication was described above, and overlaying them as shown in the figure. In this configuration, the light is transmitted only in the overlap region where transmission (T) occurs for both cells. In the R regions light will be blocked by selective reflection. A transmission profile across one such apodizer is shown in Fig. 41.27. The clear aperture of the device can be adjusted by mechanically sliding the two GCLC elements relative to each other.

2. Circular beam apodizers of large clear aperture

Geometrical constraints to liquid-crystal apodizer construction using previous designs[12] makes scaling up to apertures greater than 6 mm difficult. These difficulties are eliminated by designing an apodizer that consists of a single, homogeneous CLC fluid between a plano-convex lens with radius of curvature ρ and a plano-concave lens with radius of curvature ρ', the curved surfaces forming the inner wall. The two substrates have slightly different inner radii of curvature. Index matching between fluid and substrate lens

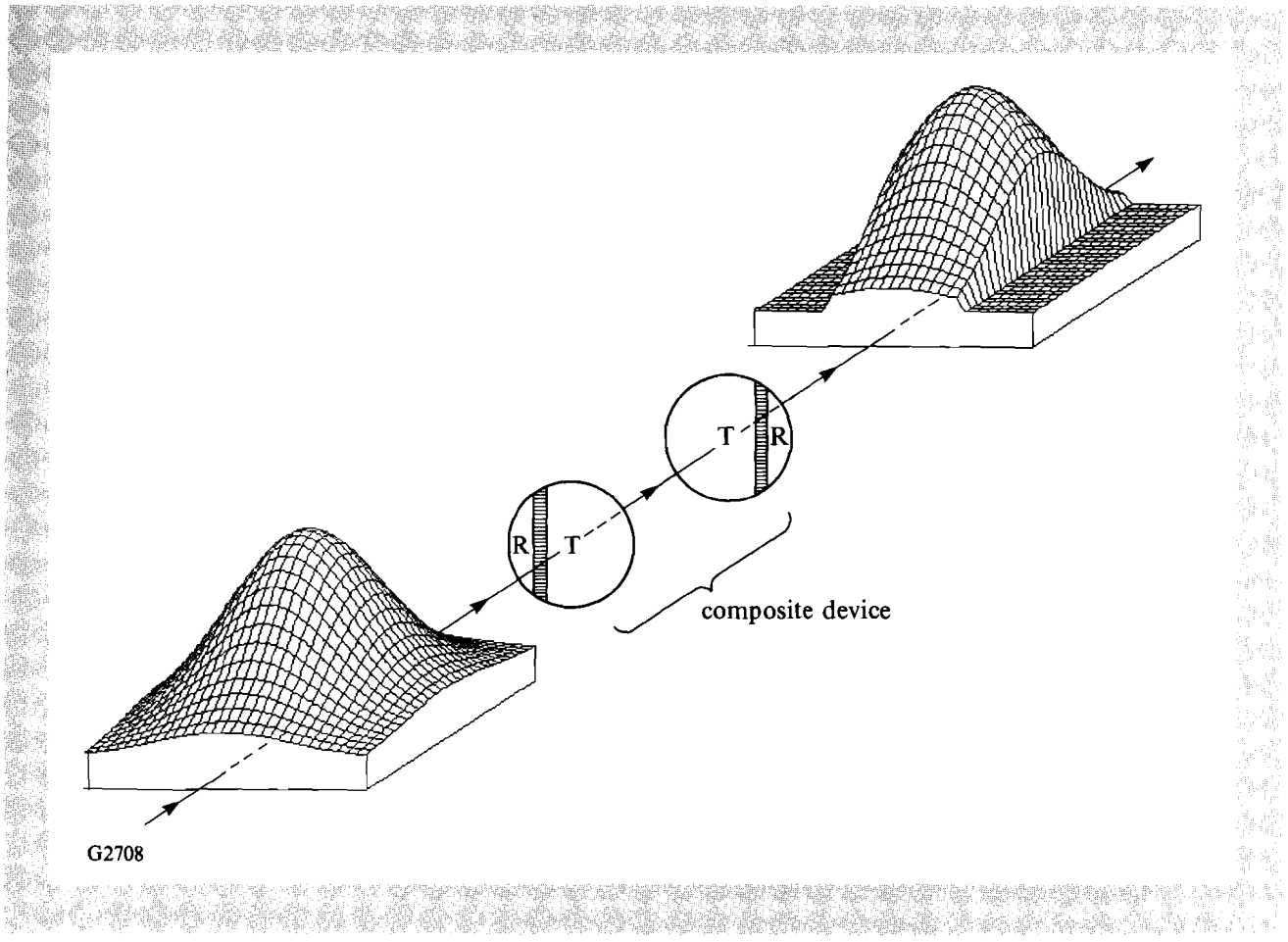

Fig. 41.26
A one-dimensional beam apodizer can be obtained by stacking a pair of two complimentary CLC cells. A variation in lateral position of the cells relative to each other allows for the adjustment of the clear aperture. In this illustration, *R* represents reflection of the incident beam, *T* represents transmission. The shaded area represents the mixing region in each element where a pitch gradient exists.

elements is important to remove focusing. This requires that the average refractive index of the substrates should be close to n_{av} of the fluid. The gap thickness between the two substrates is given by

$$L(r) = \frac{r^2}{2\rho}\left[1-\frac{\rho}{\rho'}\right] \tag{5}$$

The transmission profiles for $\rho/\rho' = 0.863$ and $\rho/\rho' = 0.9$ with $\rho = 1033.4$ mm are shown in Fig. 41.28 as two solid lines. As ρ/ρ' increases, that is, as the radii of curvature for the two substrates approach each other, the clear aperture of the apodizer increases. In this figure, the dotted lines represent

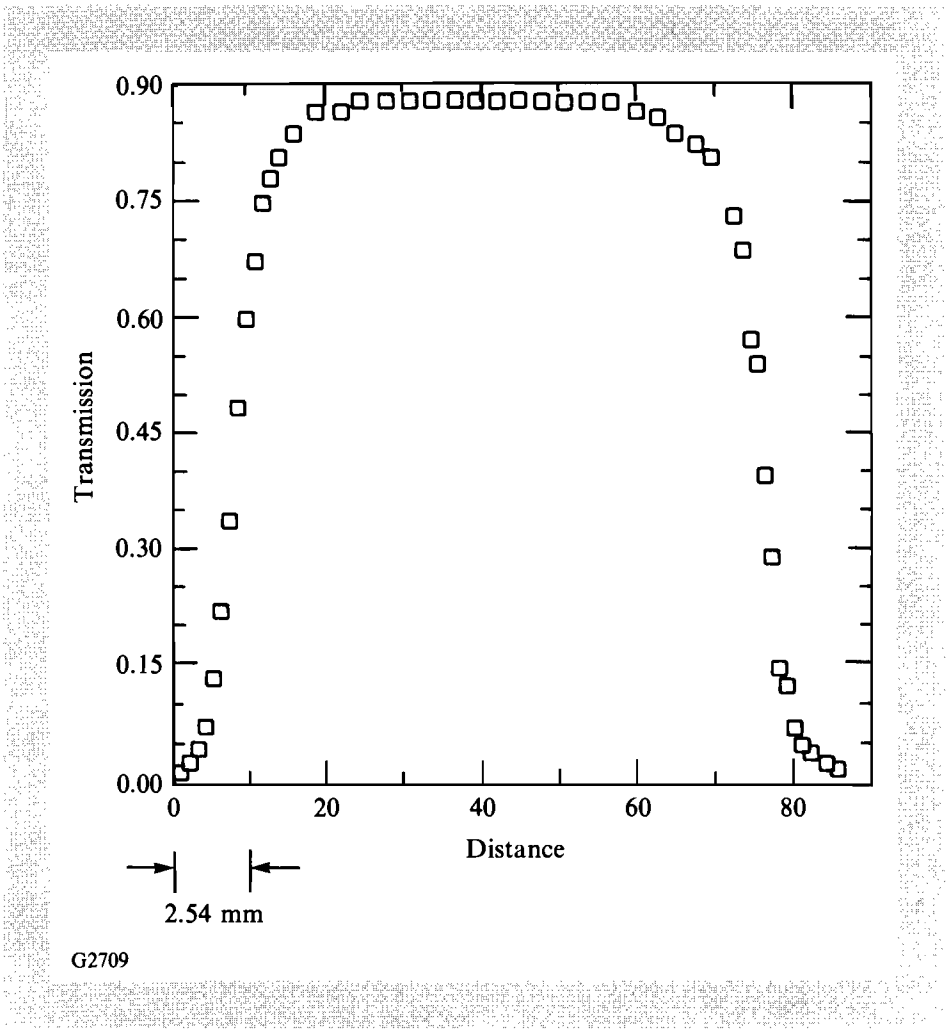

Fig. 41.27
Transmission profile of a one-dimensional apodizer. GCLC's that were annealed in the isotropic phase for 1 h and 2 h were chosen to construct the composite device.

a super-Gaussian fit to the transmission profiles. Both fits show that the order of the super-Gaussian is $N = 3.51$. As long as the CLC fluid thickness is varied according to Eq. (5), the order of the apodizer is invariant and equal to $N = 3.51$ for this design.

Two 50.8-mm-diameter substrates with ρ = 1033.4 mm and ρ' = 1197.5 mm were obtained and assembled into a cell. The air gap was filled by capillary action at 60°C with a homogeneous mixture of E7 and CB15 tuned to 1064 nm as shown in Fig. 41.29. The measured (circles) transmission for the device at 22°C and calculated (solid line) profiles as a function of radius are shown in Fig. 41.30. Super-Gaussian fits to both curves (dashed lines) give $N = 3.51$ ($r_o = 8.5$ mm) for the theoretical data and $N = 3.52$ ($r_o = 9.9$ mm) for the experimental data. Local misalignment of molecules in the CLC can cause the coupling coefficient to be lower than the theoretical value, explaining the discrepancy. In general, a super-Gaussian apodizer of order greater than 3.51 is required in high-power laser applications to maximize output energy.[1] This cannot be achieved with the simple, single-fluid concept demonstrated above, because the order N of the super-Gaussian cannot be varied. The addition of a gradient-index effect, however, permits orders greater than 3.51 to be constructed.

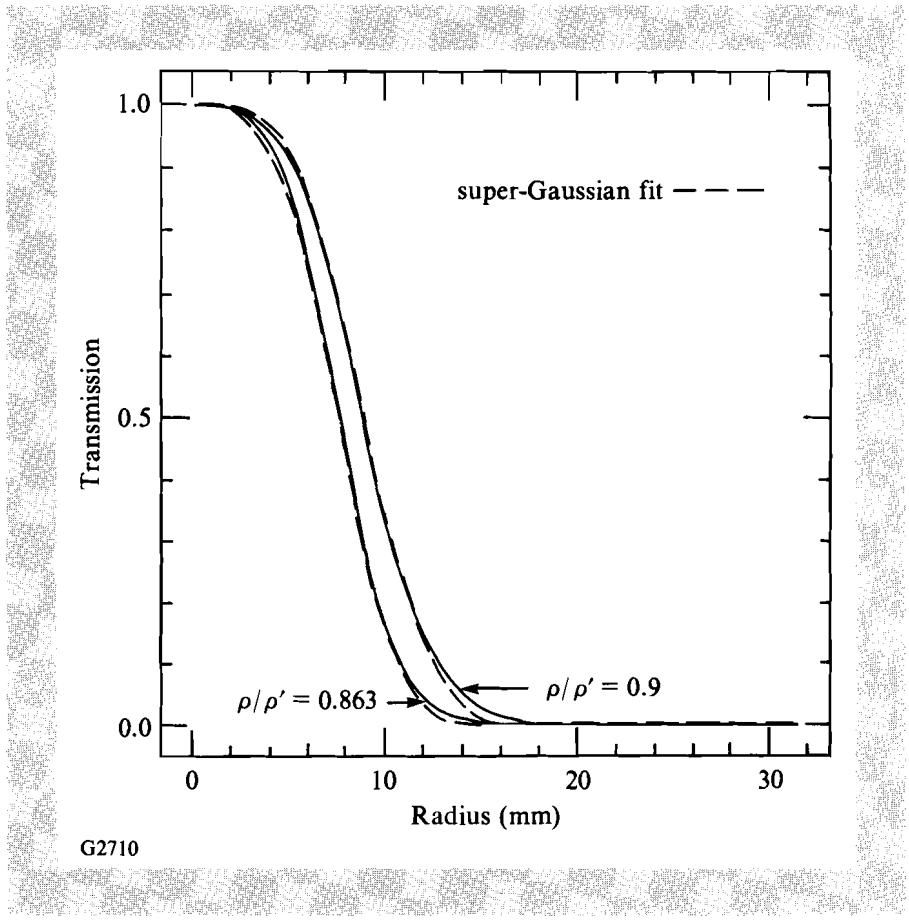

Fig. 41.28
Calculated edge-transmission profiles for two CLC beam apodizers with $\rho/\rho' = 0.863$ and $\rho/\rho' = 0.9$ (two solid lines). Here dotted lines represent super-Gaussian fits for each case.

3. Gradient-index circular apodizers

The GCLC concept can be used to construct circular apodizers with a wider range of profiles. The concept is shown in Fig. 41.31. In this figure, CLC1 has high transmission and CLC2 has high reflection at the design wavelength. The fluid-like properties of CLC's allow them to mix together and form a pitch-gradient region where the reflectivity changes from 0 to 1 outward radially from the center of the device. Good circular symmetry can be achieved by using slightly different radii of curvature for the supporting substrates so that CLC1 is drawn into the narrow gap area in the center by radial capillary action.

In order to prove the concept, two 50.8-mm-diameter substrates with $\rho = 1033.4$ mm and $\rho' = 1197.5$ mm were chosen to assemble a cell. Mixtures of ZLI1167 and CB15 (isotropic at 90°C, tuned to 910 nm) and E7 and CB15 (isotropic at 60°C, tuned to 1064 nm) were used as CLC1 and CLC2, respectively. This device is designed such that, with curved surfaces acting as the inner cell walls, the gap thickness at the inner edge of the CLC2 band is sufficient to give high reflection.

Fabrication required several steps. First, CLC1 was filled by capillary action at 90°C until it assumed a good circular symmetry at the center of the cell. The cell was then cooled to 45°C and CLC2 was loaded in very slowly, so as not to initiate mixing. CLC1 tended to resist deformation because of

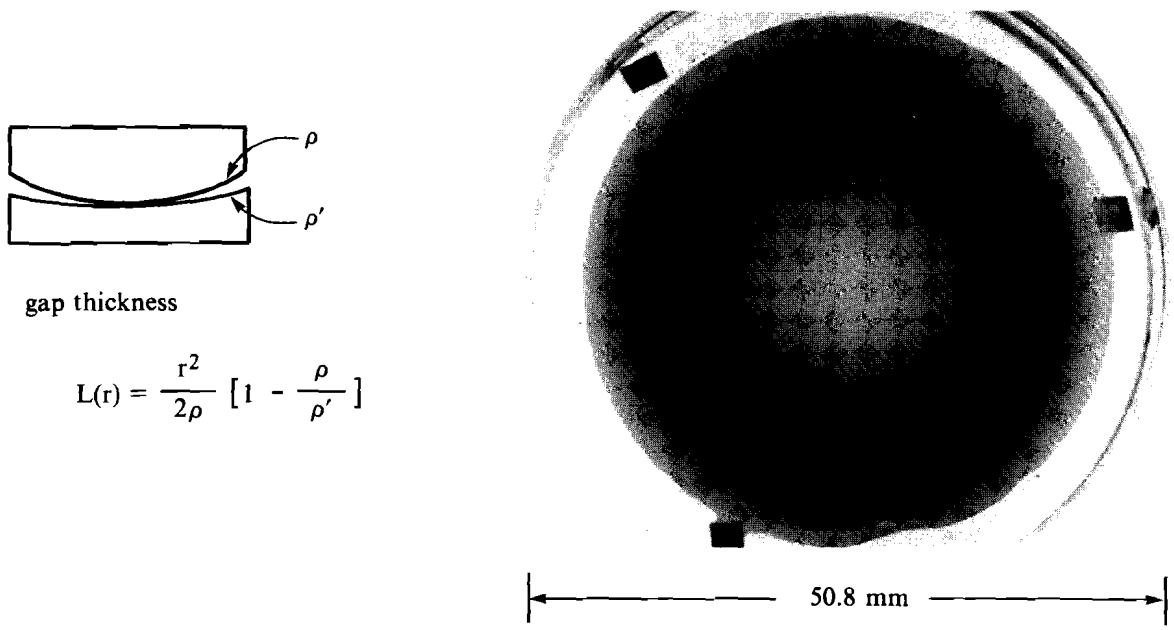

Fig. 41.29
Photograph, between linear polarizers, of a 1064-nm CLC circular beam apodizer made from off-the-shelf plano-concave/convex lenses (ρ = 1033.4 and ρ' = 1197.5). The schematic diagram indicates the assembly orientation and the resulting relationship for fluid gap L, as a function of radial dimension r.

its increased viscosity at the lower temperature. Once the filling of CLC2 was done, the temperature was increased to 90°C for a 1-h anneal in the isotropic phase of both blends. The element was then cooled to room temperature and sheared to get good alignment.

Experimental data (circles) taken at 22°C and a super-Gaussian fit (dashed line) are shown in Fig. 41.32. This apodizer profile is seen to match a super-Gaussian of order $N = 8.3$ with $r_0 = 12.4$ mm. The deviation from ideal performance in the central flat-top region, where high transmittance is required, is a result of residual reflectance at 1064 nm from the wing of the CLC1 reflection band centered at 910 nm. It can be eliminated by preparing a CLC1 blend that has a selective-reflection peak at a shorter wavelength than 910 nm. The slope at the edge of the apodizer can be changed by varying the length of time at which the filled device is thermally annealed at a constant temperature above the isotropic phase-transition temperatures of the mixtures, where the viscosities are low. A slight asymmetry to the apodizer profile seen in Fig. 41.32 is the result of a wedge inadvertently introduced by epoxy in a sealing operation.

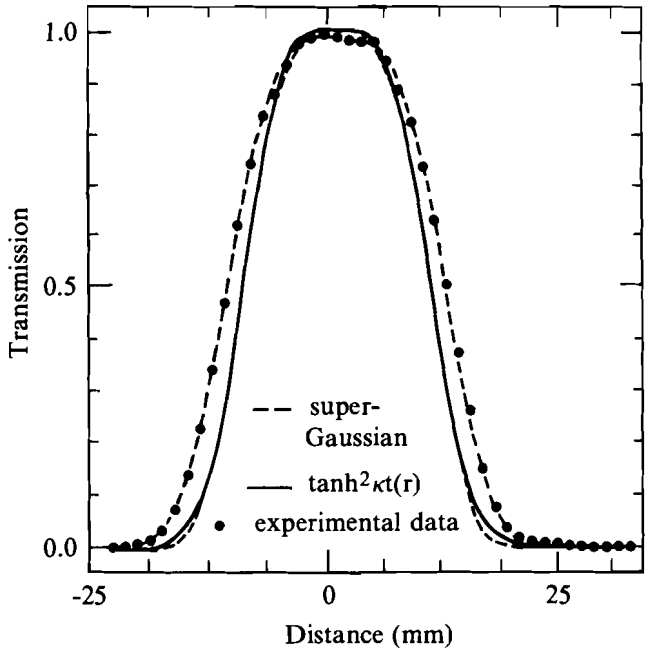

Fig. 41.30
Transmission profile at λ = 1064 nm, for a circular CLC apodizer filled with a homogeneous fluid (mixture of E7 and CB15). The solid line is the calculated transmission profile for an ideal case, the circles are the experimental results and the dotted lines represent the best super-Gaussian fit to the data (N = 3.51).

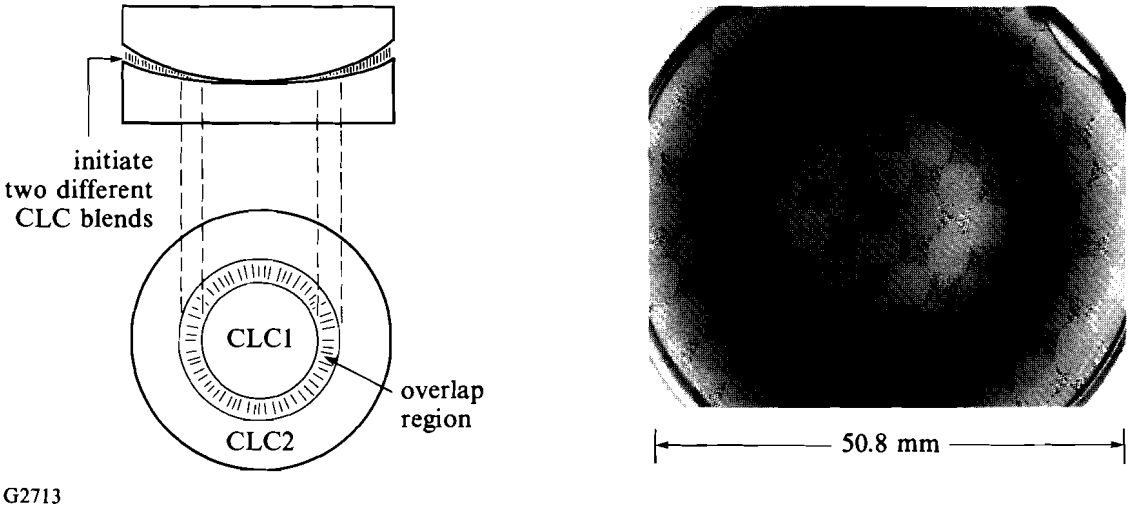

Fig. 41.31
Photograph, between two linear polarizers, of a 1064-nm GCLC beam apodizer. For this apodizer, the mixture of CB15 in ZLI1167, tuned to 910 nm is used as CLC1; the mixture of CB15 in E7, tuned to 1064 nm is used as CLC2.

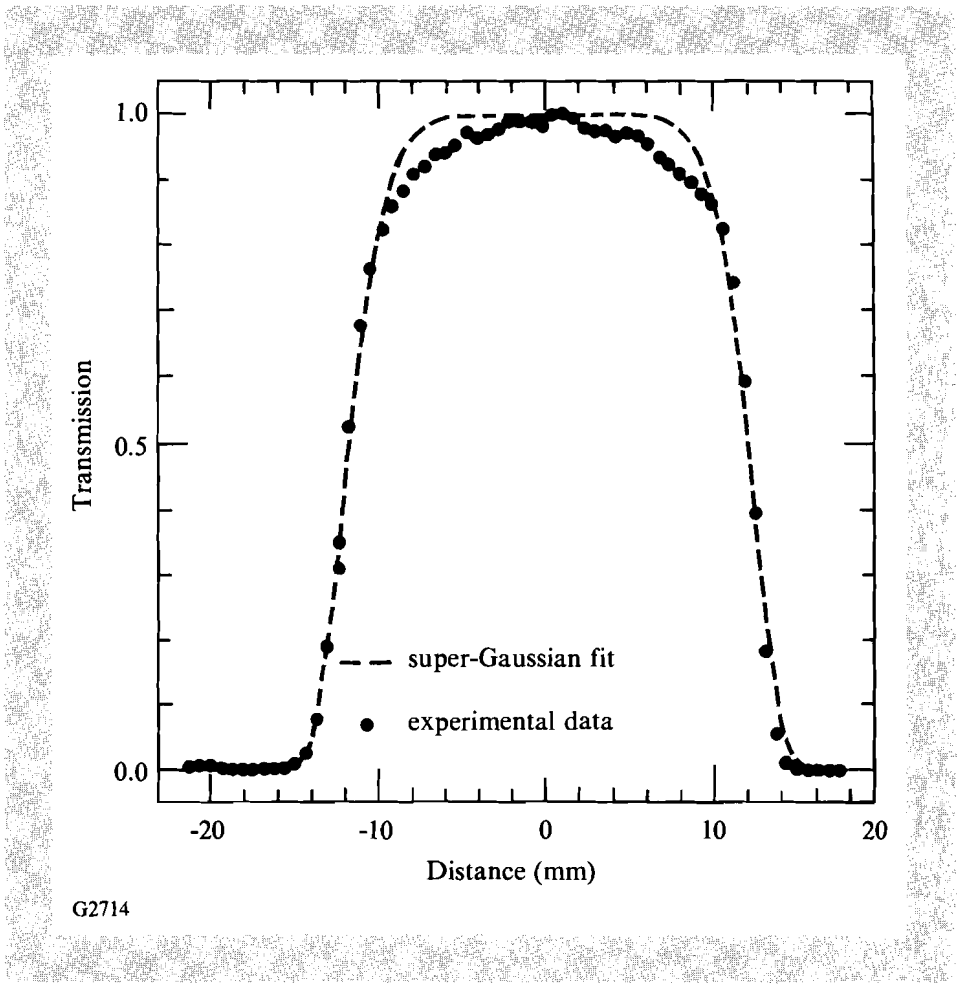

Fig. 41.32
Transmission profile of the GCLC apodizer in Fig. 41.31 at $\lambda = 1064$ nm. The circles are the experimental results and the dotted line represents the best super-Gaussian fit to the data ($N = 8.3$, $r_0 = 12.4$ mm).

Temperature changes can cause wavelength shifts to the features of liquid-crystal devices. Temperature dependence of the selective-reflection peak wavelengths for the two CLC's used to make the graded-index circular apodizer are shown in Fig. 41.33. In the temperature range of 20°C to 30°C, the selective-reflection peak wavelength is shifted 2.8 nm /°C for the mixture of E7 and CB15 and 2 nm /°C for the mixture of ZLI1167 and CB15. New chiral dopants have recently been described that could be employed to reduce temperature sensitivity of CLC mixtures.[17]

The laser-damage thresholds for GCLC apodizers depend largely upon the compounds used for blending. Since 1986 CLC devices up to 100 mm in diameter have been used as circular polarizers in more than 60 positions on OMEGA.[12] Extensive system testing of assembled polarizer elements and off-line laser-damage experiments on the fluids themselves have found that blends like CB15 in E7 have intrinsic laser-damage thresholds of about 5 J/cm^2 (1-on-1 or n-on-1 at 1054-nm, 1-ns, 3-mm spot). Fluid blends that

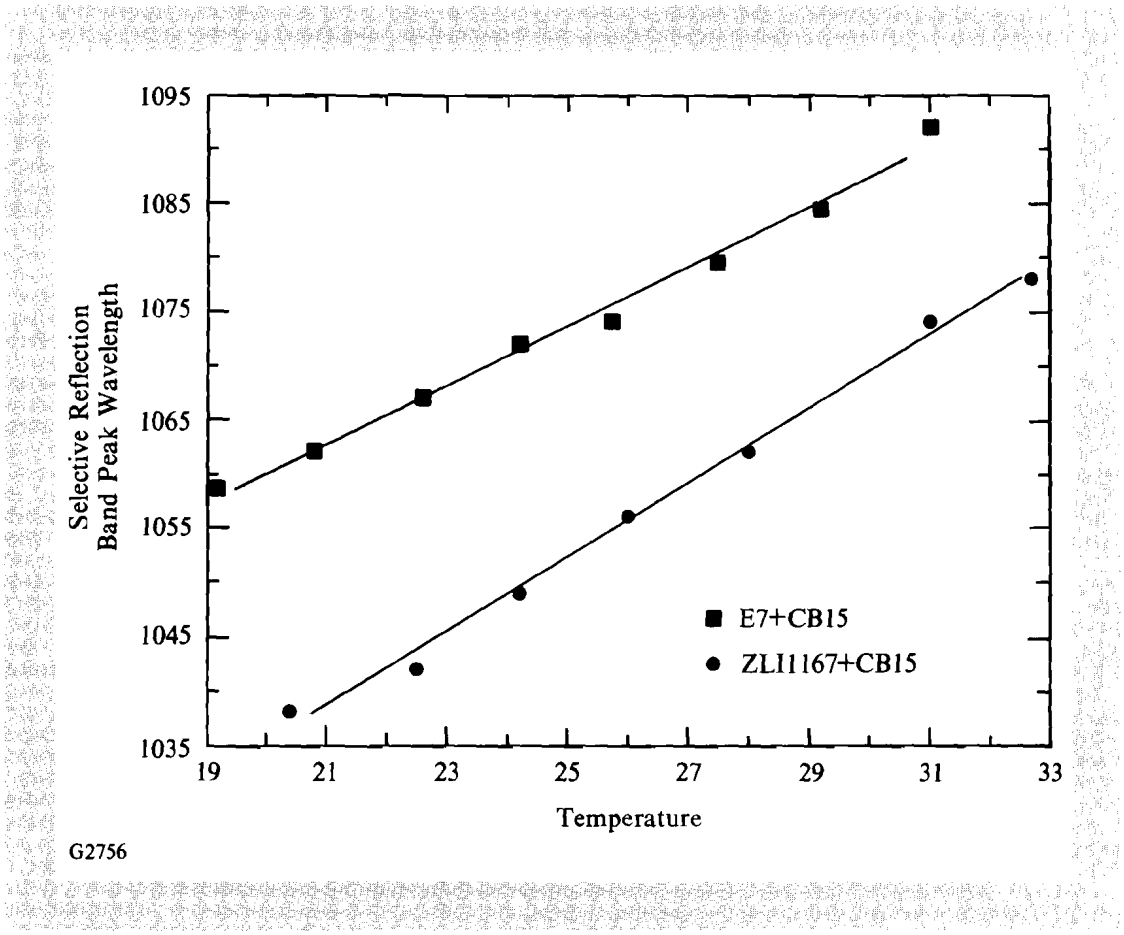

Fig. 41.33
Change in selective-reflection peak wavelength as a function of temperature for the ZLI1167 + CB15 (circles) and the E7 + CB15 mixtures (squares).

contain base nematics like ZLI1167 have recently been shown to be at least three times more resistant to bulk laser damage under identical conditions, because of their more nearly saturated chemical structure.[18] Wave-front quality has not yet been measured for these apodizers, but it should be better than $\lambda/4$ based on our previous work.[12]

Summary

We have described the design, fabrication, and characterization of laser-beam apodizers based upon gradient-index optical effects in liquid crystals. For a one-dimensional apodizer design, the clear aperture was shown to be variable by means of sliding two device elements over each other. The order of the super-Gaussian edge profile was maintained. A circular apodizer, in which the thickness variation of CLC fluid was defined by two substrates with different inner-surface radii of curvature, had a fixed-edge profile given by a super-Gaussian order of $N = 3.51$. The ability to vary N in this design was established by using the mixing property of liquid crystals to create a gradient-index optical effect. For this application it is important to have weak anchoring only, at either one or both of the inner surfaces of the apodizer, to prevent any discontinuity in structure.

ACKNOWLEDGMENT

The author would like to express his thanks to Daewoo Heavy Industries, Ltd., of Incheon, Korea, for their financial support during this work. This work was supported by the U.S. Army Research Office under contract DAAL03-86-K-0173, the U.S. Department of Energy Division of Inertial Fusion under agreement No. DE-FC03-85DP40200, and by the Laser Fusion Feasibility Project at the Laboratory for Laser Energetics, which has the following sponsors: Empire State Electric Energy Research Corporation, New York State Energy Research and Development Authority, Ontario Hydro, and the University of Rochester.

REFERENCES

1. V. R. Costich and B. C. Johnson, *Laser Focus* **10**, 43 (1974).
2. A. Penzkofer and W. Frohlich, *Opt. Commun.* **28**, 197 (1979).
3. Y. Asahara and T. Izumitani, U.S. Patent 4,108,621 (August 22, 1978).
4. G. Dubé, *Advanced Laser Technology and Applications*, edited by L. Esterowitz, *Proc. Soc. Photo-Opt. Instrum. Eng.* **335**, 10 (1982).
5. V. I. Kryzhanovskii *et al., Sov. J. Quantum Electron.* **13**, 194 (1983).
6. A. J. Campillo, B. Carpenter, B. E. Newnam, and S. L. Shapiro, *Opt. Commun.* **10**, 313 (1974).
7. E. W. S. Hee, *Opt. Laser Technol.* **7**, 75 (1975).
8. S. B. Arifzhanov *et al., Sov. J. Quantum Electron.* **11**, 745 (1981).
9. G. Dubé, *Opt. Commun.* **12**, 344 (1974).
10. J.-C. Diels, *Appl. Opt.* **14**, 2810 (1975).
11. B. J. Feldman and S. J. Gitomer, *Appl. Opt.* **16**, 1484 (1977).
12. S. D. Jacobs, K. A. Cerqua, K. L. Marshall, A. Schmid, M. J. Guardalben, and K. J. Skerrett, *J. Opt. Soc. Am. B* **5**, 1962 (1988).
13. J. L. Fergason, *Liquid Crystals: Proceedings of the International Conference on Liquid Crystals*, Kent State University, 16–20 August 1965, edited by G. H. Brown, G. J. Dienes, and M. M. Labes (Gordon and Breach, New York, 1967), p. 89.
14. J. C. Lee, J. H. Kelly, D. L. Smith, and S. D. Jacobs, *IEEE J. Quantum Electron.* **24**, 2238 (1988).
15. P. D. de Gennes, *The Physics of Liquid Crystals* (Oxford, Claredon, 1974), p. 264.
16. *Ibid*, p. 240.
17. F. Leenhouts, S. Kelly, and A. Villiger, *Appl. Phys. Lett.* **54**, 696 (1989).
18. M. Guardalben, A. Schmid, S. D. Jacobs, and S. H. Chen, presented at the First International Symposium on Nonlinear Optical Polymers, Natick, MA, 13–14 June 1988. See also: M. Guardalben, A. Bevin, K. Marshall, and A. Schmid, *Proceedings, 20th Annual Symposium on Optical Materials*, Boulder, CO, 26 October 1988, in press.

2.B Laser Ionization of Noble Gases by Coulomb Barrier Suppression

Introduction

The ionization of atoms and ions in high-intensity laser fields allows a study of atomic structure under extreme conditions. The electric field of the laser can approach or even exceed the electric field binding an electron to a nucleus. At even higher laser intensities, electron motion in the laser field can become relativistic.

We have studied the ionization of five noble gases with 1.053-μm, 1-ps laser pulses[1] using the tabletop terawatt laser (T^3) (see Ref. 2), developed at LLE. Experimentally measured intensities ranging from mid-10^{13} W/cm^2 to mid-10^{16} W/cm^2 were used with charge states up to He^{2+}, Ne^{6+}, Kr^{8+}, Ar^{8+}, and Xe^{12+} observed. It was found that the "appearance" or "threshold" intensity (intensity at which ionization of a particular charge state commences) was a function of both the ionization potential and the charge of the ionic state. The ionization occurred completely in the tunneling regime and was accurately predicted by a simple model of Coulomb barrier suppression due to the laser electric field [barrier suppression ionization (BSI)].[1]

Experiments involving the interaction of atoms with intense laser fields have traditionally been divided into two regimes: multiphoton and tunneling. In the former, laser ionization can be described by perturbation theory, while in the latter ionization can be described as an ac tunneling process. These regions can be quantitatively separated by introducing the Keldysh γ parameter[3]

$$\gamma = \sqrt{\frac{E}{2\Phi}}\ , \tag{1}$$

where E is the ionization potential of the atom or ion and Φ is the ponderomotive potential of the laser,

$$\Phi(\mathrm{eV}) = \frac{e^2\mathcal{E}^2}{4m\omega^2} 9.33\times10^{-14} \times I(W/\mathrm{cm}^2) \times \lambda^2(\mu\mathrm{m}), \tag{2}$$

where $\mathcal{E}$ is the laser electric field. In the multiphoton regime, $\gamma > 1$, the laser field can be treated perturbatively while in the tunneling regime, $\gamma < 1$, the laser field is treated quasistatically.

Most laser-induced ionization experiments performed to date have observed ion production in the multiphoton regime.[4–9] Work in the tunneling regime has been, up to now, confined to 10-μm-wavelength CO_2 lasers.[10–12] Thus, these results represent the first observations of ionization in the tunneling regime for near-visible wavelengths, and the highest charge states observed in this regime.

We will first discuss the laser characteristics and the experimental apparatus. A presentation of the data and a comparison to the BSI theory follows.

Experiments

The laser used for these experiments is an Nd:glass laser based on the concept of chirped pulse amplification and compression (CPAC).[2] The laser is operated at the fundamental wavelength of 1.053 μm, with a nominal pulse width of 1 ps and a bandwidth of ~20 Å. Using f/5 optics (20-cm-focal-length lens) intensities up to mid-10^{16} W/cm^2 were obtained. The intensity is known with a relative shot-to-shot uncertainty of 25% and an absolute uncertainty of a factor of ~2.

The experiment is set up to detect noble gas ions produced by very intense laser fields. A single gas, or mixture of gases, is introduced into a vacuum chamber by means of a leak valve. The target gas (He, Ne, Ar, Kr, and/or Xe) uniformly back-fills the chamber to a pressure of typically 5×10^{-6} Torr. A liquid-nitrogen-trapped diffusion pump is used to obtain a background pressure of 1×10^{-8} Torr that is sufficient to eliminate almost all impurity signals from our ion spectra.

The ion spectra are obtained with a standard time-of-flight spectrometer that has an extraction field of 800 V/cm and a field-free drift length of 30 cm. The ions are detected with a dual microchannel plate (MCP) operated at 1000 V/plate that gives a total signal gain of ~10^6. The spectra are recorded with a digitizing oscilloscope that allows resolution of charge states up to Xe^{13+}.

After the spectra are stored, the individual ion peaks are integrated to determine the number of ions detected in each charge state. These values are then plotted versus the laser intensity for that shot. The graphs, shown in Figs. 41.34(a) and 41.34(b), plot the number of ions detected versus laser intensity for xenon and neon. The solid curves are from theoretical calculations and will be discussed in the following section. For clarity, data that reflect detector saturation effects have been removed from these graphs.

The appearance intensity of each of the various charge states seen is defined as the lowest intensity at which that charge state can be detected above the background detector noise. Since the slope of the data curves is very steep for low ion number, the exact choice of the number of ions detected is unimportant. A value of 10 ions detected has been chosen to determine the appearance intensities. A comparison of the appearance intensities for the various gases demonstrates a significant atomic species dependence on the ionization rates as can be seen in Fig. 41.35. All charge states detected were produced in the regime of $\gamma < 1$, which indicates that we are operating exclusively in the tunneling regime.

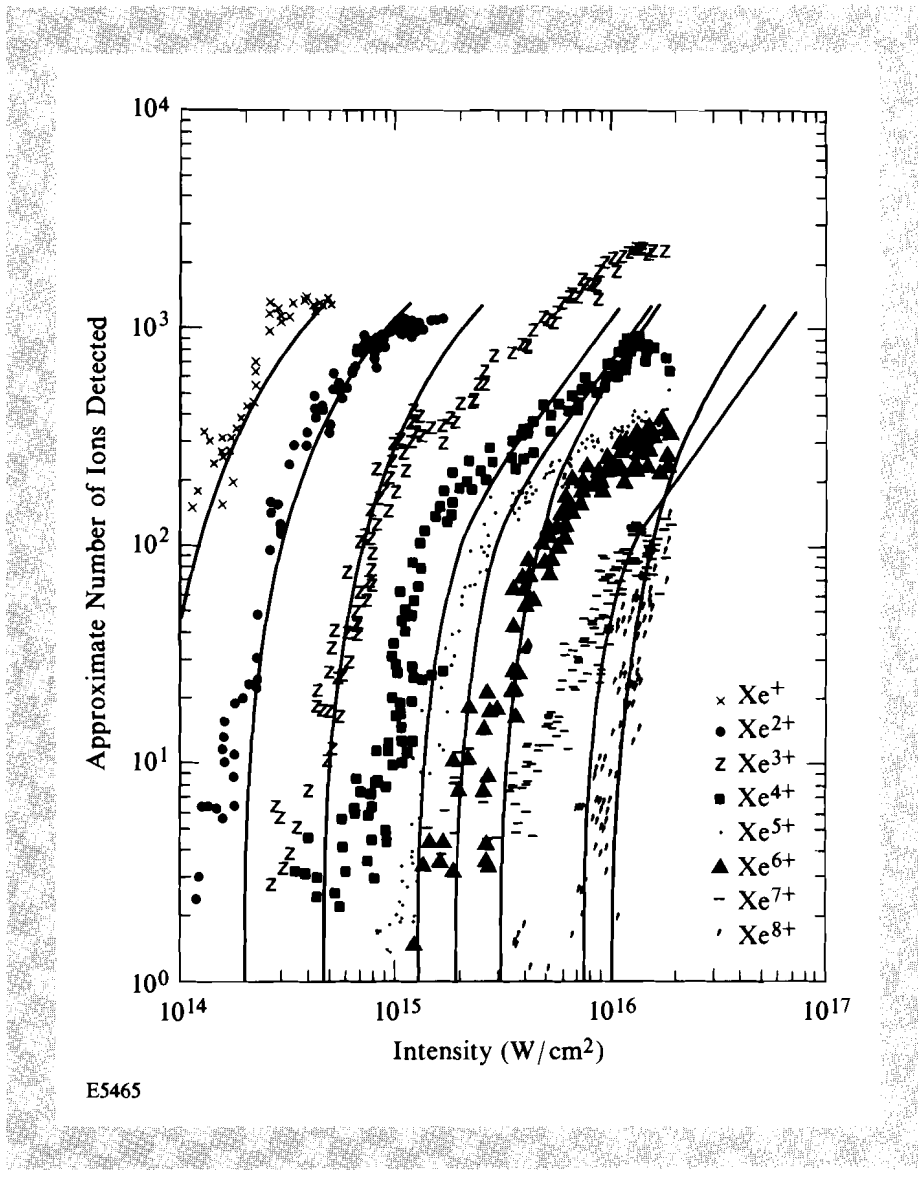

Fig. 41.34(a)
Xenon ion-production rate as a function of laser intensity. The theoretical curves are from BSI theory with no shift in intensity. ($P = 5 \times 10^{-6}$ Torr).

Barrier Suppression Ionization

A simple one-dimensional model of ionization consists of a superposition of the Coulomb potential with a static electric field.[13] The laser electric field suppresses the Coulomb field thereby creating a barrier over which an electron can escape. The resulting potential is written as

$$V(x) = -\frac{Ze^2}{|x|} - e\,\mathcal{E}x\,. \tag{3}$$

This potential has a relative maximum located at x_{max} that can easily be found by setting $\partial V(x)/\partial x = 0$ and solving for x_{max}. Equating $V(x_{max})$ to the

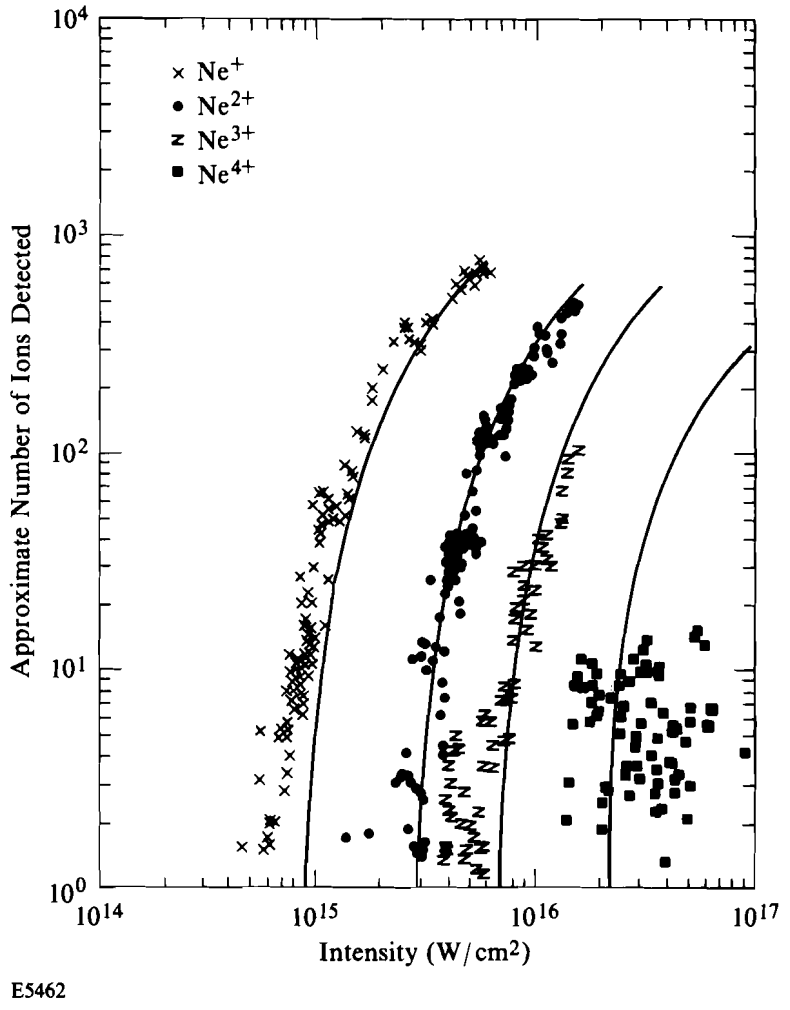

Fig. 41.34(b)
Neon ion-production rate as a function of laser intensity. The theoretical curves are from BSI theory with no shift in intensity. ($P = 2.5 \times 10^{-6}$ Torr).

ionization potential (E) of the atom or ion permits us to find the critical electric field that is necessary to allow the bound electron to escape without tunneling. The critical electric field is

$$\mathcal{E}^2 = \frac{E^4}{16e^2Z^2} \cdot \tag{4}$$

Setting the magnitude of the laser electric field equal to this critical field strength results in a laser intensity that can be considered to be the appearance intensity

$$I_{\text{app}} = \frac{cE^4}{128\pi e^6 Z^2} \cdot \tag{5}$$

In a Coulombic system, the ionization potential is dependent on the ionic charge Z and the principal quantum number n: $E = (m_e Z^2\alpha^2c^2)/(2n^2)$. However, for the calculations used here, electron-shielding effects are accounted for by using values of E that have been determined either experimentally or by use of more complicated calculations than those given in the Bohr model. Appearance intensities calculated in this manner are compared to the experimentally determined ones in Fig. 41.36. In all cases the theory and experiment agree within the experimental uncertainties.

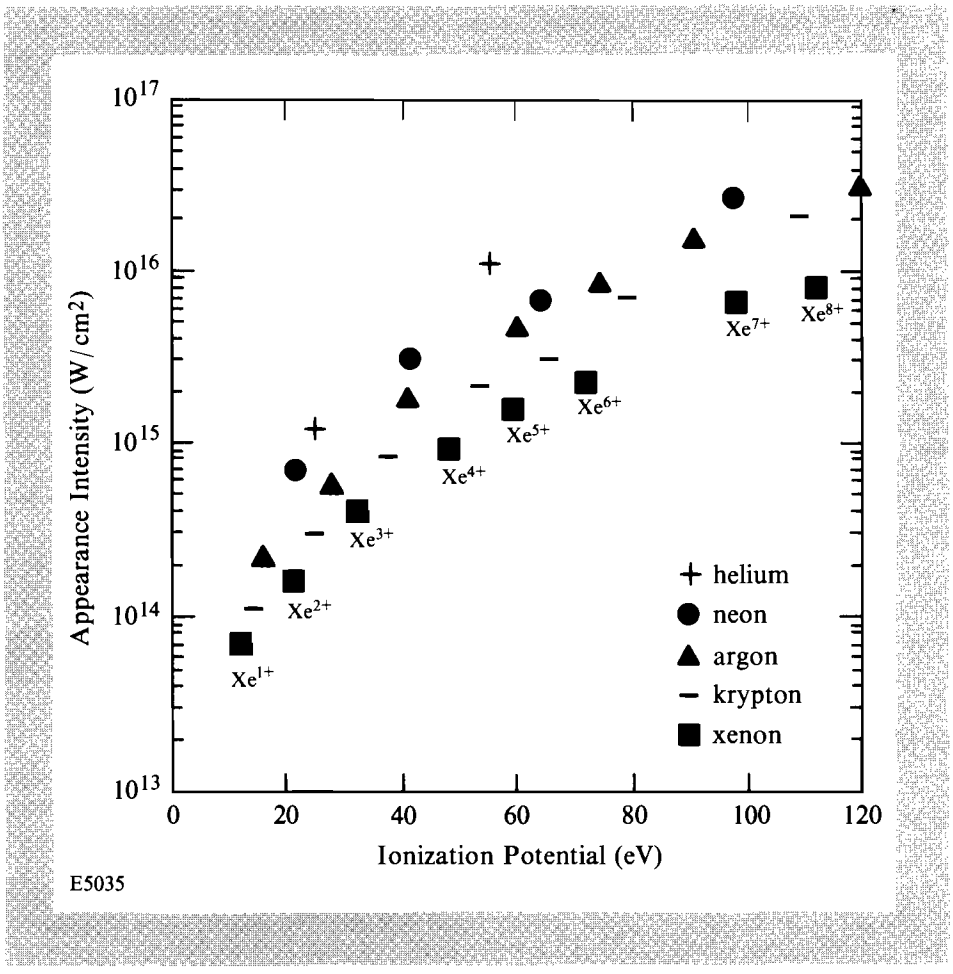

Fig. 41.35
Appearance intensity of each charge state versus the sequential ionization potential showing a clear species dependence present.

In addition to comparing appearance intensities, theoretical ion-production curves are obtained by integrating the coupled rate equations for the number of ions in each charge state. The spatial and temporal dependence of the intensity, and consequently of the ionization rates, is also accounted for in the calculation. The integration is performed by finding the volume of each iso-intensity shell and then propagating a laser pulse through that volume. The number of particles in each shell is conserved so saturation effects are

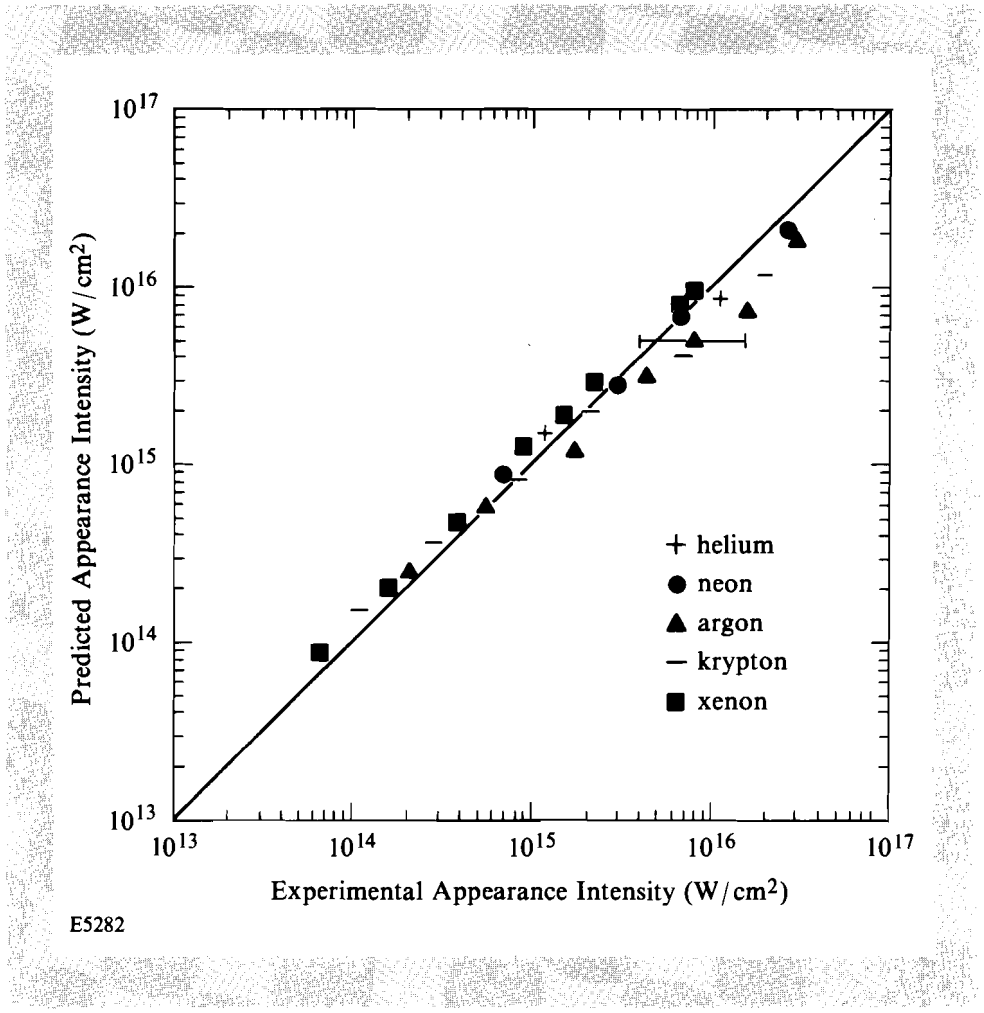

Fig. 41.36
Comparison of measured appearance intensities and those obtained from BSI theory [Eq. (5)]. A typical experimental error bar is shown.

accounted for. The intensity distribution is modeled as temporally Lorentzian and spatially Gaussian.[14] The volume of an iso-intensity shell is

$$\text{Volume} = \frac{\pi z_R w_o^2}{2}\left\{\frac{4(c_1 - c_2)}{3} + \frac{2\left(c_1^3 - c_2^3\right)}{9} - \frac{4}{3}\left[\tan^{-1}(c_1) - \tan^{-1}(c_2)\right]\right\}, \tag{6}$$

where w_o is the $1/e$ diameter of the focal spot, $z_R = \pi w_o^2 / \lambda$ is the Rayleigh range of the focus, and

$$c_j = R\sqrt{(I_o - I_j)/I_j}$$

with I_o being the peak laser intensity and I_j the intensity of shell j. The calculation assumes only sequential ionization occurs.

The ion spectra are calculated for BSI theory by assuming that the ionization probability is unity for $I \geq I_{app}$ and zero for $I < I_{app}$. The resulting BSI theory curves shown in Fig. 41.34 use a one-parameter fit, this being the shift in the vertical scale that simply accounts for spectrometer efficiency. There has been no shift along the intensity scale for theoretical curves shown in Fig. 41.34; thus, these are effectively zero-parameter fits to the ionization. As can be seen, the agreement is excellent.

Summary/Discussion

In summary, we present results of high-intensity laser ionization of noble gases. It is found that for a 1-ps laser pulse at $\lambda = 1.053$ μm, the ionization rates are strongly species dependent, unlike results obtained with a 1-ps, 586-nm laser.[7] Additionally, all ion production occurs in the tunneling regime ($\gamma < 1$), contrary to results obtained with a 50-ps laser pulse at the same wavelength that clearly shows ion production occurring in the multiphoton regime.[9]

The measured ion production is well predicted by a Coulomb barrier suppression ionization theory.

ACKNOWLEDGMENT

This work was supported by the National Science Foundation Grant PHY-8822730. Additional support was provided by the U.S. Department of Energy Division of Inertial Fusion under agreement No. DE-FC03-85DP40200 and by the Laser Fusion Feasibility Project at the Laboratory for Laser Energetics, which has the following sponsors: Empire State Electric Energy Research Corporation, New York State Energy Research and Development Authority, Ontario Hydro, and the University of Rochester.

REFERENCES

1. S. Augst, D. Strickland, D. D. Meyerhofer, S. L. Chin, and J. H. Eberly, *Phys. Rev. Lett.* **63**, 2212 (1989).
2. P. Maine, D. Strickland, P. Bado, M. Pessot, and G. Mourou, *IEEE J. Quantum Electron.* **QE-24**, 398 (1988).
3. L. V. Keldysh, *Sov. Phys. JETP* **20**, 1307 (1965).
4. T. S. Luk *et al.*, *Phys. Rev. A* **32**, 214 (1985).
5. C. K. Rhodes, *Phys. Scr.* **T17**, 193 (1987).
6. S. L. Chin, C. Rolland, P. B. Corkum, and P. Kelly, *Phys. Rev. Lett.* **61**, 153 (1988).
7. M. D. Perry, O. L. Landen, A. Szöke, and E. M. Campbell, *Phys. Rev. A* **37**, 747 (1988).
8. M. D. Perry, A. Szöke, O. L. Landen, and E. M. Campbell, *Phys. Rev. Lett.* **60**, 1270 (1988).
9. A. L'Huillier, L. A. Lompré, G. Mainfray, and C. Manus, *J. Phys. B* **16**, 1363 (1983).
10. F. Yergeau, S. L Chin, and P. Lavigne, *J. Phys. B* **20**, 723 (1987).

11. S. L. Chin, W. Xiong, and P. Lavigne, *J. Opt. Soc. Am. B* **4**, 853 (1987).

12. S. L. Chin and W. Xiong, *Fundamentals of Laser Interactions II*, edited by F. Ehlotzky (Springer-Verlag, Berlin, 1989), p. 80.

13. BSI is a simplified version of work done by M. Brewczyk and M. Gajda, *J. Phys. B* **21**, L383 (1988); E. J. Valeo, S. M. Susskind, C. R. Oberman, and I. B. Berstein, *Bull. Am. Phys. Soc.* **34**, 2099 (1989).

14. D. T. Strickland, Ph.D. thesis, University of Rochester, 1989.

Section 3
NATIONAL LASER USERS FACILITY NEWS

The first quarter of FY90 user activity consisted of support for groups from the University of Maryland and the University of Florida. This consisted of meetings with LLE staff and diagnostic checkout on the OMEGA target chamber.

J. Moreno from the University of Maryland conducted a checkout of a time-dependent XUV spectrograph on the OMEGA target chamber. This instrument will be used to measure the XUV spectra at various times from an imploding glass microballoon. This is a McPIGS instrument that will be used in conjunction with SPEAXS to measure the time dependence of x-ray emission over a broad energy region. The targets for these measurements consist of glass microballoons with varying thicknesses of CH overcoats. These experiments are to be done during the second quarter of FY90.

C. Hooper from the University of Florida visited LLE to coordinate the investigation of argon-filled plastic microballoons. A series of targets with varying pressures and shell thicknesses are planned to study high-density implosions. This work is being done in collaboration with LLE scientists and relies on instrumentation fielded by LLE staff. A new batch of LLE-made plastic shells that are matched to the DPP's on the OMEGA target chamber are being manufactured and tested for retention of argon gas.

ACKNOWLEDGMENT

This work was supported by the U.S. Department of Energy Division of Inertial Fusion under agreement No. DE-FC03-85DP40200.

Section 4
LASER SYSTEM REPORT

4.A GDL Facility Report

The first quarter of FY90 saw the continuation of four main experimental programs. The programs are x-ray laser, shine-through, optical probing/ interaction, and Thomson-scattering experiments. Significant progress was achieved in all of these projects, and results were reported at the Monterey Conference on Laser Plasma Interactions and the November meeting of the American Physical Society. In preparation for these meetings, additional laser shots were performed by extending the operation schedule to evenings and Saturdays.

A summary of GDL operations this quarter follows:

Beamline Test, Calibration, Tuning, and Laser Alignment Shots	346
Target Shots	
Shine-through	71
X-Ray Laser	49
X-Ray Lithography	3
Probe Beam	86
Thomson Scattering	51
TOTAL	606

ACKNOWLEDGMENT

This work was supported by the U.S. Department of Energy Division of Inertial Fusion under agreement No. DE-FC03-85DP40200 and by the Laser Fusion Feasibility Project at the Laboratory for Laser Energetics, which has the following sponsors: Empire State Electric Energy Research Corporation, New York State Energy Research and Development Authority, Ontario Hydro, and the University of Rochester.

4.B OMEGA Facility Report

During this quarter, activities were split between laser enhancements and full-scale target shots. Beam-smoothing and power-balance activities continued with the goal of improving and equalizing the spatial and temporal characteristics of each of the 24 beams. Target drive-uniformity requirements have tightened tolerances on beam profiles and laser-diagnostic calibration and stressed the need for increased diagnostic capability.

After several months of successful operation of SSD on OMEGA at 3 GHz, it was decided that the best way to improve the smoothing of the laser beam was to increase the frequency at which the laser beam was phase modulated. This would have the effect of decreasing the time required for the laser beam to reach its asymptotic level of smoothing. The design goal was a factor-of-3 increase in frequency to 9 GHz.

The major task was then to design and build a lithium niobate microwave phase modulator at 9 GHz that would produce about the same bandwidth, i.e., 3 Å to 5 Å, that the 3-GHz modulator had produced. The basic difficulty was designing a resonant microwave modulator at 9 GHz that would use a crystal of roughly the same dimensions (several millimeters) as those used for the 3-GHz modulator, in order to keep the laser intensity below the damage limit. It had been observed during the design of the 3-GHz modulator that the operation of the resonator was greatly dependent upon the shape of the lithium niobate crystal, not just upon the capacitance of the crystal, which would have been expected. It was believed at that time that the internal crystal resonant modes might have been responsible for these observations. It was decided to make use of this effect in the design of the 9-GHz resonator. The basic idea was to have a resonator, loaded with the capacitance of the crystal, be resonant at a frequency close enough to an internal resonant mode of the lithium niobate to efficiently couple energy into it. At 9 GHz the free-space wavelength is about 3 cm, which means that inside the lithium niobate, with a dielectric constant of 27 or 41 depending on the orientation, the wavelength is of the order of 5 or 6 mm in the two directions. This then places a rough upper bound, i.e., approximately one wavelength, on the dimensions of the crystal. Many designs were tried; the design that finally worked was a rectangular parallelepiped of lithium niobate as a capacitive load at the end of a tunable resonant-transmission-line cavity. With loose-loop coupling to the cavity, a bandwidth of between 3 Å and 4 Å was measured with a pulsed microwave input power of about 40-kW peak at a frequency of 8.45 GHz and 400-ns pulse width.

This preliminary design has now been installed on the OMEGA system and will be used for a short period of time until a new waveguide-coupled cavity is finished, which will have better coupling characteristics and should provide greater bandwidth for the same power input.

Power-balance monitoring has been improved by an automated installation of 24 calorimeters that now provides energy-sensing system-calibration checks on a daily basis. Also, a 24-beam UV streak camera has been installed and is operational on OMEGA. This new diagnostic was brought online to measure the state of power balance on OMEGA and, as of the end of the quarter, it was undergoing final calibration and optimization.

Two incremental improvements to the rod amplifier subsystems during this quarter have had a beneficial impact on the power balance of the system. First, a new alignment fixture ensures accuracies of ±200 μm in rod alignment measurements and allows for all 54 rod amplifiers to be tested for positioning in a single day. Second, new O-ring seals on the rod amplifiers have been installed that can withstand the intense flash-lamp radiation, thereby decreasing the possibility of contamination due to leaking coolant.

In support of the experimental campaigns, a regenerative ring-laser system has been built in the driver line of OMEGA. The resultant 0.5-J IR pulse is converted to 4ω and is to be used as a timing fiducial on x-ray streak cameras, as well as other time-resolved target diagnostics. Target experiments utilizing this fiducial are planned for early next quarter.

A summary of laser shots on OMEGA follows:

Driver Line	85
Laser Test	110
Target	109
Software Test/Other	62
TOTAL	366

ACKNOWLEDGMENT

This work was supported by the U.S. Department of Energy Division of Inertial Fusion under agreement No. DE-FC03-85DP40200 and by the Laser Fusion Feasibility Project at the Laboratory for Laser Energetics, which has the following sponsors: Empire State Electric Energy Research Corporation, New York State Energy Research and Development Authority, Ontario Hydro, and the University of Rochester.

PUBLICATIONS AND CONFERENCE PRESENTATIONS

Publications

S. Augst, D. Strickland, D. D. Meyerhofer, S. L. Chin, and J. H. Eberly, "Tunneling Ionization of Noble Gases in a High-Intensity Laser Field," *Phys. Rev. Lett.* **63**, 2212–2215 (1989).

J. M. Chwalek, D. R. Dykaar, J. F. Whitaker, T. Y. Hsiang, G. A. Mourou, D. K. Lathrop, S. E. Russek, and R. A. Buhrman, "Picosecond Transient Propagation Studies on Thin-Film Y-Ba-Cu-O Transmission Lines," in *Ultrafast Phenomena VI*, Vol. 48, edited by T. Yajima, K. Yoshihara, C. B. Harris, and S. Shionoya (Springer-Verlag, Berlin, Heidelberg, 1988), pp. 201–204.

T. Y. Hsiang, J. F. Whitaker, R. Sobolewski, S. Martinet, and L. P. Golob, "High-Frequency Characterization of Superconducting Transmission Structures from Picosecond Transient Measurements" (invited paper), in *Proceedings of the 1989 International Superconductivity Electronics Conference* (ISEC '89), Tokyo, Japan, 13 June 1989, pp. 510–515.

S. D. Jacobs, T. E. Gunderman, and K. L. Marshall, "Liquid Crystal Optics," *Opt. News*, 39 (1989).

A. M. Kadin, W. R. Donaldson, P. H. Ballentine, and R. Sobolewski, "Nonequilibrium Hot-Electron Transport in Optically Irradiated YBCO Films," *PHYSICA C* **162-164**, 387–388 (1989).

H.-J. Kong, M. D. Wittman, and H. Kim, "New Shearing Interferometer for Real-Time Characterization of Cryogenic Laser Fusion Targets," *Appl. Phys. Lett.* **55**, 2274–2276 (1989).

J. C. Lambropoulos, M. R. Jolly, C. A. Amsden, S. E. Gilman, M. J. Sinicropi, D. Diakomihalis, and S. D. Jacobs, "Thermal Conductivity of Dielectric Thin Films," *J. Appl. Phys.* **66**, 4230–4242 (1989).

F. J. Marshall, S. A. Letzring, C. P. Verdon, S. Skupsky, R. L. Keck, J. P. Knauer, R. L. Kremens, D. K. Bradley, T. Kessler, J. Delettrez, H. Kim, J. M. Soures, and R. L. McCrory, "Cryogenic-Laser-Fusion-Target Implosion Studies Performed with the OMEGA UV Laser System," *Phys. Rev. A* **40**, 2547–2557 (1989).

R. L. McCrory and C. P. Verdon, "Computer Modeling and Simulation in Inertial Confinement Fusion," *Inertial Confinement Fusion*, edited by A. Caruso and E. Sindoni (Societa Italiana di Fisica, Italy, 1989), pp. 83–124.

R. L. McCrory, J. M. Soures, C. P. Verdon, S. Skupsky, T. J. Kessler, S. A. Letzring, W. Seka, R. S. Craxton, R. Short, P. A. Jaanimagi, M. Skeldon, D. K. Bradley, J. Delettrez, R. L. Keck, H. Kim, J. P. Knauer, R. L. Kremens, and F. J. Marshall, "Laser Compression and Stability in Inertial Confinement Fusion," *Plasma Phys. and Controlled Fusion* **31**, 1517–1533 (1989).

S. Skupsky, R. W. Short, T. Kessler, R. S. Craxton, S. Letzring, and J. M. Soures, "Improved Laser-Beam Uniformity Using the Angular Dispersion of Frequency-Modulated Light," *J. Appl. Phys.* **66**, 3456–3462 (1989).

F. W. Smith, S. Gupta, H. Q. Le, M. Frankel, V. Diadiuk, M. A. Hollis, D. R. Dykaar, G. A. Mourou, T. Y. Hsiang, and A. R. Calawa, "Picosecond GaAs-Based Photoconductive Optoelectronic Detectors," *Appl. Phys. Lett.* **54**, 890–892 (1989).

J. F. Whitaker, T. B. Norris, G. Mourou, T. C. Sollner, W. D. Goodhue, X. J. Song, and L. F. Eastman, "Tunneling-Time Measurements of a Resonant Tunneling Diode," in *Ultrafast Phenomena VI*, Vol. 48, edited by T. Yajima, K. Yoshihara, C. B. Harris, and S. Shionoya (Springer-Verlag, Berlin, Heidelberg, 1988), pp. 185–188.

X. Zhou, T. Y. Hsiang, and R. J. D. Miller, "Monte Carlo Study of Photo-Generated Carrier Transport in GaAs Surface Space Charge Fields," *J. Appl. Phys.* **66**, 3066–3073 (1989).

Forthcoming Publications

G. Banas, H. E. Elsayed-Ali, F. V. Lawrence, Jr., and J. M. Rigsbee, "Laser Shock-Induced Mechanical and Microstructural Modification of Welded Maraging Steel," to be published in *Journal of Applied Physics*.

S. H. Batha, D. D. Meyerhofer, and A. Simon, "Enhanced Scattering from Laser-Plasma Interactions," to be published in *Physical Review*.

T. Boehly, B. Yaakobi, D. Shvarts, D. Meyerhofer, P. Audebert, J. Wang, M. Russotto, B. Boswell, R. Epstein, R. S. Craxton, and J. M. Soures, "X-Ray Laser Experiments Using Double Foil Nickel Targets," to be published in *Applied Physics* .

B. Boswell, D. Shvarts, T. Boehly, and B. Yaakobi, "X-Ray Laser Beam Propagation in Double-Foil Targets," to be published in *Physics of Fluids*.

H. C. Chen, G. Mourou, and R. Knox, "Time-Resolved Electron Diffraction from Pulse-Excited Crystalline Gold Films," to be published in the *Proceedings of 1989 Materials Research Society Fall Meeting: Beam-Solid Interactions*, Boston, MA, 27 November - 2 December 1989; and in *Physical Review Letters*.

P. C. Cheng, V. H-K. Chen, H. Kim, and R. E. Pearson, "An EPI-Fluorescent Spinning-Disk Confocal Microscope," to be published in the *Proceedings of the 47th Annual Meeting of Electron Microscopy Society of America* (EMSA), Austin, TX, 14–18 August 1989.

W. R. Donaldson, A. M. Kadin, P. H. Ballentine, and M. Shoup III, "Optically Activated High Temperature Superconductor Opening Switches," to be published in the *Proceedings of the 7th IEEE Pulsed Power Conference*, Monterey, CA, 11–14 June 1989.

W. R. Donaldson, L. Kingsley, M. Weiner, A. Kim, and R. Zeto, "Electro-Optic Imaging of the Internal Fields in a GaAs Photoconductive Switch," to be published in *Applied Physics Letters*.

H. E. Elsayed-Ali, "Hot Electron Relaxation in Metals," to be published in *High Energy Density Physics with Subpicosecond Laser Pulses* (Optical Society of America, Washington, DC, 1989).

H. E. Elsayed-Ali, "Comments on 'Thermal Response of Metals to Ultrashort-Pulse Laser Excitation'," to be published in *Physical Review Letters*.

H. E. Elsayed-Ali and J. W. Herman, "An Ultrahigh Vacuum Picosecond Laser-Driven Electron Diffraction System," to be published in *Review of Scientific Instruments*.

E. M. Epperlein, "Electron Kinetics in Laser-Driven Inertial Confinement Fusion," to be published in the *Proceedings of the Topical Conference on Research Trends in Nonlinear and Relativistic Effects in Plasmas*, San Diego, CA, 5–8 February 1990.

M. Y. Frankel and T. Y. Hsiang, "Picosecond Transient Behavior of Pseudomorphic High Electron Mobility Transistor—Simulations," to be published in *IEEE Transactions on Electron Devices*.

M. Y. Frankel, D. R. Dykaar, T. Y. Hsiang, K. H. Duh, and P. C. Chao, "Non-Invasive, Picosecond Transient Characterization of Pseudomorphic High Electron Mobility Transistor (HEMT)," to be published in *IEEE Transactions on Electron Devices*.

R. Q. Gram, M. D. Wittman, C. Immesoete, H. Kim, R. S. Craxton, N. Sampat, S. Swales, G. Pien, J. M. Soures, and H. Kong, "Uniform Liquid-Fuel Layer Produced in a Cryogenic Inertial Fusion Target by a Time-Dependent Thermal Gradient," to be published in *Journal of Vacuum Science and Technology*.

C. Immesoete, L. Forsley, and H. Kim, "Computer-Assisted Microballoon Selection for Laser Fusion Targets," to be published in the *Proceedings of the Forth Conference*, Rochester, NY, 19–23 June 1989.

Conference Presentations

The following presentations were made at the OSA Annual Meeting, Orlando, FL, 15–20 October 1989:

J. E. Hayden and S. D. Jacobs, "Stress Measurements of Transparent Optical Materials Using a Beam Scanning Modulated Transmission Ellipsometer."

T. Kessler and S. Skupsky, "Laser Beam Smoothing by Exploitation of Light Parameters."

The following presentations were made at the American Vacuum Society 36th National Symposium & Topical Conference, Boston, MA, 23–27 October 1989:

R. Q. Gram, M. D. Wittman, C. Immesoete, H. Kim, R. S. Craxton, N. Sampat, S. Swales, G. Pien, J. M. Soures, and H.-J. Kong, "Uniform Liquid-Fuel Layer Produced in a Cryogenic Inertial Fusion Target by a Time-Dependent Thermal Gradient."

C. Immesoete, S. Scarantino, H. Kim, and L. Forsley, "Computer-Assisted Microballoon Selection for Inertial Confinement Targets."

M. D. Wittman, H. Kim and H.-J. Kong, "New Shearing Interferometer for Real-Time Characterization of Cryogenic Laser Fusion Targets.

S. D. Jacobs, "Thin Films for High Power Lasers," presented at a Physics Department seminar, Arizona State University, Tempe, AZ, 3 November 1989.

J. C. Lambropoulos and S. -S. Hwang, "Film Thermal Conductivity and Laser Damage Resistance of Optical Thin Films," presented at the symposium on Electro-Optics and Nonlinear Optics, 1st International Ceramic Science and Technology Congress, Anaheim, CA, 31 October – 3 November 1989.

The following presentations were made at the Ninth Workshop of Laser Interaction and Related Plasma Phenomena Matter, Monterey, CA, 6–10 November 1989.

T. Boehly, J. Wang, B. Yaakobi, R. S. Craxton, and R. Epstein, "Observation of Gain in Ne-Like Germanium and Other X-Ray Laser Developments at LLE."

D. K. Bradley, T. Boehly, D. L. Brown, J. Delettrez, W. Seka, and D. Smith, "Early-Time 'Shine-Through' in Laser Irradiated Targets."

The following presentations were made at the Thirty-First Annual Meeting of the Division of Plasma Physics of the American Physical Society, Anaheim, CA, 13–17 November 1989:

T. Boehly, D. Bradley, D. L. Brown, J. Knauer, W. Seka, D. Smith, and C. P. Verdon, " 'Shine-Through' Early-Time Phenomena in Laser Fusion Targets."

D. K. Bradley, J. Delettrez, P. A. Jaanimagi, C. P. Verdon, J. D. Kilkenny, and P. Bell, "Time-Resolved X-Ray Imaging of Implosion Experiments on the OMEGA Laser System."

D. L. Brown, W. Seka, and T. Boehly, "Self-Focusing and Dielectric Laser Breakdown."

R. S. Craxton, C. Darrow, G. E. Busch, and E. F. Gabl, "Image Distortion as a Diagnostic of Refraction in Long-Scale-Length Plasmas."

J. Delettrez, C. P. Verdon, D. K. Bradley, and P. A. Jaanimagi, "The Role of the Rayleigh-Taylor Instability in Spherical Burnthrough Experiments at 0.35 μm."

E. M. Epperlein, C. J. McKinstrie, and G. G. Luther, "Laser Beam Filamentation in Direct-Drive ICF Targets."

R. Epstein, S. Skupsky, T. J. Kessler, W. P. Castle, N. Sampat, and S. Swales, "Anticipated Improvement in Laser Beam Uniformity Using Distributed Phase Plates with Quasi-Random Patterns."

P. A. Jaanimagi, J. Kelly, R. Keck, W. Seka, and R. Saunders, "Pulse Shape and Power Balance Measurements on OMEGA."

R. L. Keck, J. P. Knauer, S. Letzring, S. Morse, W. D. Seka, and J. M. Soures, "Improvements to Energy and Power Balance on OMEGA."

J. P. Knauer, R. L. McCrory, J. M. Soures, C. P. Verdon, F. J. Marshall, S. A. Letzring, S. Skupsky, T. J. Kessler, R. L. Kremens, H. Kim, J. Delettrez, R. L. Keck, and D. K. Bradley, "Implosion of Gas Filled Glass Microballoons with the OMEGA Laser."

R. Kremens and M. Russotto, "A Small Array of Single-Hit Neutron Detectors."

S. Letzring, C. P. Verdon, J. P. Knauer, S. Skupsky, and R. Kremens, "Effects on Target Implosion Experiments on OMEGA with Variations in Laser Bandwidth Utilizing Smoothing by Spectral Dispersion (SSD)."

G. G. Luther and C. J. McKinstrie, "Ponderomotive Filamentation In Counter-Propagating Geometry."

F. J. Marshall, S. A. Letzring, C. P. Verdon, J. P. Knauer, J. M. Soures, R. L. McCrory, M. Wittman, H. Kim, R. L. Keck, D. K. Bradley, P. A. Jaanimagi, W. Seka, T. Kessler, and S. Skupsky, "Cryogenic Target Experiments Performed with the OMEGA UV Laser System."

P. W. McKenty, S. Skupsky, D. K. Bradley, W. Seka, and C. P. Verdon, "Numerical Determination of the Effects of Laser Power Balance on the Levels of Illumination Nonuniformities."

C. J. McKinstrie and G. G. Luther, "The Filamentation of Counter-Propagating Waves in a Finite Collisional Plasma."

D. D. Meyerhofer, S. H. Batha, H. Chen, Y. -H. Chuang, J. Delettrez, R. Epstein, M. C. Richardson, S. Uchida, and B. Yaakobi, "Characterization of Plasmas Produced By Intense, 1-ps, Laser Pulses."

G. Pien, F. J. Marshall, S. A. Letzring, C. Dulnikowski, and A. Hauer, "Positioner for Laser Fusion Diagnostics Used on the OMEGA."

M. Russotto and R. Kremens, "Analysis of Current-Mode Neutron Time-of-Flight Detector Data for ICF Implosions."

W. Seka, D. L. Brown, T. Boehly, D. Bradley, T. Balasubramanian, R. Bahr, "Self-Focusing in Glass and Transparent Plastic Coatings in Multi-Layer Targets Relevant to Laser Fusion."

R. W. Short, "Self-Focusing and Smoothing by Spectral Dispersion."

A. Simon, "Studies of the Saturated Plasma Wave Regime in the Enhanced Thomson Model of Raman Scattering."

S. Skupsky, "Highly Smooth Laser Beams for ICF, Using Bandwidth Dispersion Techniques," (invited talk).

J. M. Soures, J. Kelly, S. Morse, J. Knauer, S. Letzring, R. L. McCrory, and W. Seka, "The Influence of Amplifier Gain Saturation on OMEGA Power Balance."

C. P. Verdon, J. P. Knauer, D. K. Bradley, J. Delettrez, P. A. Jaanimagi, R. L. Keck, R. L. Kremens, S. Letzring, F. J. Marshall, R. L. McCrory, S. Skupsky, and J. M. Soures, "Theoretical Interpretation of OMEGA Glass Ablator Implosion Experiments."

B. Yaakobi, T. Boehly, J. Wang, R. Epstein, and R. S. Craxton, "Observation of X-Ray Gain in Collisionally Excited Germanium Targets."

The following presentations were made at the Materials Research Society Fall Meeting, Boston, MA, 27 November – 2 December 1989:

H. C. Chen, G. A. Mourou, and R. Knox, "Time-Resolved Electron Diffraction from Pulse-Excited Crystalline Gold Films," Symposium A: Beam-Solid Interactions: Physical Phenomena.

S. H. Chen, M. L. Tsai, and S. D. Jacobs, "Thermotropic Chiral Nematic Polymers as Optical Materials."

D. Y. Park, W. Seka, and L. Ying, "Mono-Mode Operation of an Imaging Unstable Resonator Using Nd:YLF as Active Medium," presented at the International Conference on Lasers '89, New Orleans, LA, 3–8 December 1989.

ACKNOWLEDGMENT

The work described in this volume includes current research at the Laboratory for Laser Energetics, which is supported by Empire State Electric Energy Research Corporation, New York State Energy Research and Development Authority, Ontario Hydro, the University of Rochester, and the U.S. Department of Energy Division of Inertial Fusion under agreement No. DE-FC03-85DP40200.